Interaction Notes
Note 542
July 20, 1998

On Identifying Conducting Objects Using Low Frequency Magnetic Fields Theory and Measurements

Lloyd S. Riggs, Jon E. Mooney, Daniel E. Lawrence
Electrical Engineering Department
Auburn University

J. Thomas Broach and Anh H. Trang
U.S. Army NVSED
Ft. Belvoir, Virginia

Abstract

This note addresses identification of conducting objects based on their response to low frequency magnetic fields. Real time identification was carried out in a laboratory setting on seven simple geometries consisting of aluminum and copper cylinders, and an aluminum ring, block, and square cylinder. The low frequency transfer function of these objects was measured in a concentric coaxial coil configuration. Data was taken for both cardinal and arbitrary orientations of the magnetic field with respect to the planes of symmetry of the objects (i.e. for different polarizations). The distinct negative real axis poles (singularities) associated with each object formed the basis for our real-time identification algorithm. Several different techniques were explored to extract poles from the measured data including: 1.) Prony's Method, 2.) Matrix Pencil Method, 3.) Differential Corrections, and a 4.) Genetic Algorithm. We compare and contrast the performance of these methods when the data is contaminated with white Gaussian noise (WGN) and demonstrate that the differential corrections method yields estimates of the singularities with variance approaching that of the Cramer-Rao lower bound. We also demonstrate through simple examples that when the difference between two competing sum-of-damped-exponential models (one with fewer poles than the other) approaches the standard deviation of the noise, the pole extraction methods mentioned above could only extract the poles from the simpler model - the one with fewer poles. Recognizing the identification problem as one of inference from incomplete information, calling for a full application of probability theory, we employ Bayes theorem to develop a generalized likelihood ratio test (GLRT) as a solution to the M-ary hypothesis testing problem of interest here. Lastly, the performance of the GLRT detector is examined as a function of the number of poles assigned to each object and as a function of the organization of the pole library with respect to polarization. Best performance, measured through Monte Carlo simulation presented in terms of percent correct identification versus signal-to-noise ratio, was obtained with a single pole per object per orientation.

Contents

1. Introduction

In the past, attempts to use low frequency electromagnetic induction (EMI) techniques for military and humanitarian demining efforts and for the removal of unexploded ordnance (UXO) have met with limited success due in large part to the many false alarms generated by metallic clutter. For example, the Army's only fielded mine detector, the AN/PSS-12, is quite sensitive and can detect mines with metallic content substantially below the gram level. Unfortunately, however, in highly cluttered environments the detector is rendered useless, for all intents and purposes. In short, a metal detector is not a mine detector! Some effort is underway today to exploit the quasi-magnetostatic response characteristics of metallic objects in order to distinguish between mines and metallic clutter. Baum in Interaction Note 499 [1] has demonstrated, within the framework of the singularity expansion method (SEM) [2], that low frequency scattering from permeable and highly conducting objects is characterized by natural frequencies that are negative and real. Equivalently, the time domain response is characterized by a sum of weighted exponentials. Unique correspondence between an objects and its singularities forms the basis for identification and therefore clutter rejection. Aptly enough, the term Magnetic Singularity Identification (MSI) has been applied to techniques employing this identification methodology [3].

A clear exposition of the physics of quasi-magnetostatic scattering, as presented in Note 499 [1], although certainly necessary, does not alone provide a sufficient foundation upon which to construct a solution to the clutter problem. We adopt the point of view that the problem is really one of inference from incomplete information, calling for a full application of probability theory. For example, object response measurements are unavoidably contaminated by noise. If the measured response is contaminated by additive white Gaussian noise (WGN) , an increase in the standard deviation of the noise will eventually result in an inability to distinguish among objects or between object classes based on their measured signatures. In short, the physics of the problem tells us the characteristics of the signature in the absence of noise (provides the model) while probability theory, through the application of Bayes Theorem, instructs us as to exactly how the data should be manipulated so as to *optimally* choose between or among the hypotheses of interest (e.g. a mine is present, a mine is not present) [7, 8, 17]. We point out that other researchers have successfully applied a Bayesian-theoretic approach to the landmine detection problem using EMI data from both time- and frequency-domain sensors. The work presented here differs from the above in that we have examined the M-ary hypothesis problem (which of a set of M mines is present) whereas previous researchers have concentrated on the binary hypothesis problem (mine or no-mine question). Additionally, the work presented here addresses the impact that polarization issues have on the identification process. Finally, this work and that previously mentioned should be compared to other less rigorous discrimination methods reported elsewhere [9].

In the following section, the phenomenology associated with low-frequency magnetic field scattering

from conducting objects is reviewed, and the measurement apparatus and procedures are presented. Section 3 addresses the challenges that exist and techniques used in extracting real poles from measured data. Four pole extraction methods are compared, and a statistical characterization in terms of the variance of the estimated model parameters is presented. Section 4 presents the GLRT used in the identification algorithm. The identification algorithm's performance depends heavily on the organization of poles in the library and the signal-to-noise ratio (SNR) of the measured data. The final section of the paper will demonstrate the varying performances of the identification algorithm in noise for different pole library organizations.

2. Phenomenology

In this section we briefly review low frequency scattering from finitely conducting bodies with the end goal being a description of the test apparatus employed in our real-time identification experiments. Fortunately, Baum [1] and others [4, 3] have already provided a particularly cogent description of the relevant phenomenology. We borrow from these works here and refer the reader to the exhaustive list of references therein.

Metallic object detection and identification depend on one's ability to sense the magnetic field radiated by eddy currents induced on and within a metallic object by an applied excitatory magnetic field. Two methods are commonly used to excite eddy currents and sense the resulting scattered magnetic fields: 1.) the pulse induction method (a time domain technique) and 2.) a frequency domain or continuous wave (CW) technique.

With pulse-induction methods, an electric current flowing through a transmit coil establishes a magnetic field in nearby conducting objects. The waveform shape of the excitatory current often includes abrupt transitions to zero (e.g. square or triangle waveforms). When the excitatory current and corresponding magnetic field are extinguished, eddy currents are established throughout the object in accordance with Faraday's law of induction and the geometry and constitutive parameters of the object [3]. As elaborated upon later, eddy currents decay *exponentially* at a rate varying, approximately, inversely with object conductivity and some characteristic dimension of the object squared [3]. A sensing coil, often located concentrically with the transmit coil, is used to detect the decaying magnetic field radiated by the eddy currents. Some pulse-induction systems are designed to minimize direct coupling between transmit and receive coils so that only target-radiated magnetic fields are measured [5]. In this case, a band-limited target impulse response may be obtained by deconvolving the incident waveform from the receive coil response.

CW methods employ sinusoidal excitation currents that induce sinusoidal eddy currents resulting in sinusoidal scattered magnetic fields. With zero coupling between transmit and receive coils, the amplitude and phase of the receive coil signal relative to that of the transmit coil yields the object's transfer function at frequency f.

Figure 2.1 shows the experimental test setup used in our real-time metallic object identification demonstration. The setup consist of a Hewlett Packard 89410A vector signal analyzer, Tektronix TM502A current probe, Analog Devices 524AD instrumentation amplifier, and coaxially positioned solenoidal excitation and receive coils. The measurement technique described here follows closely to that found in [10]. Swept frequency excitation provided by the vector analyzer drives a sinusoidal current through the exterior solenoid producing an axially-directed sinusoidal magnetic field that is approximately uniform within the excitatory coil. The receive coil has its axis coincident with that of the transmit coil and consists of N

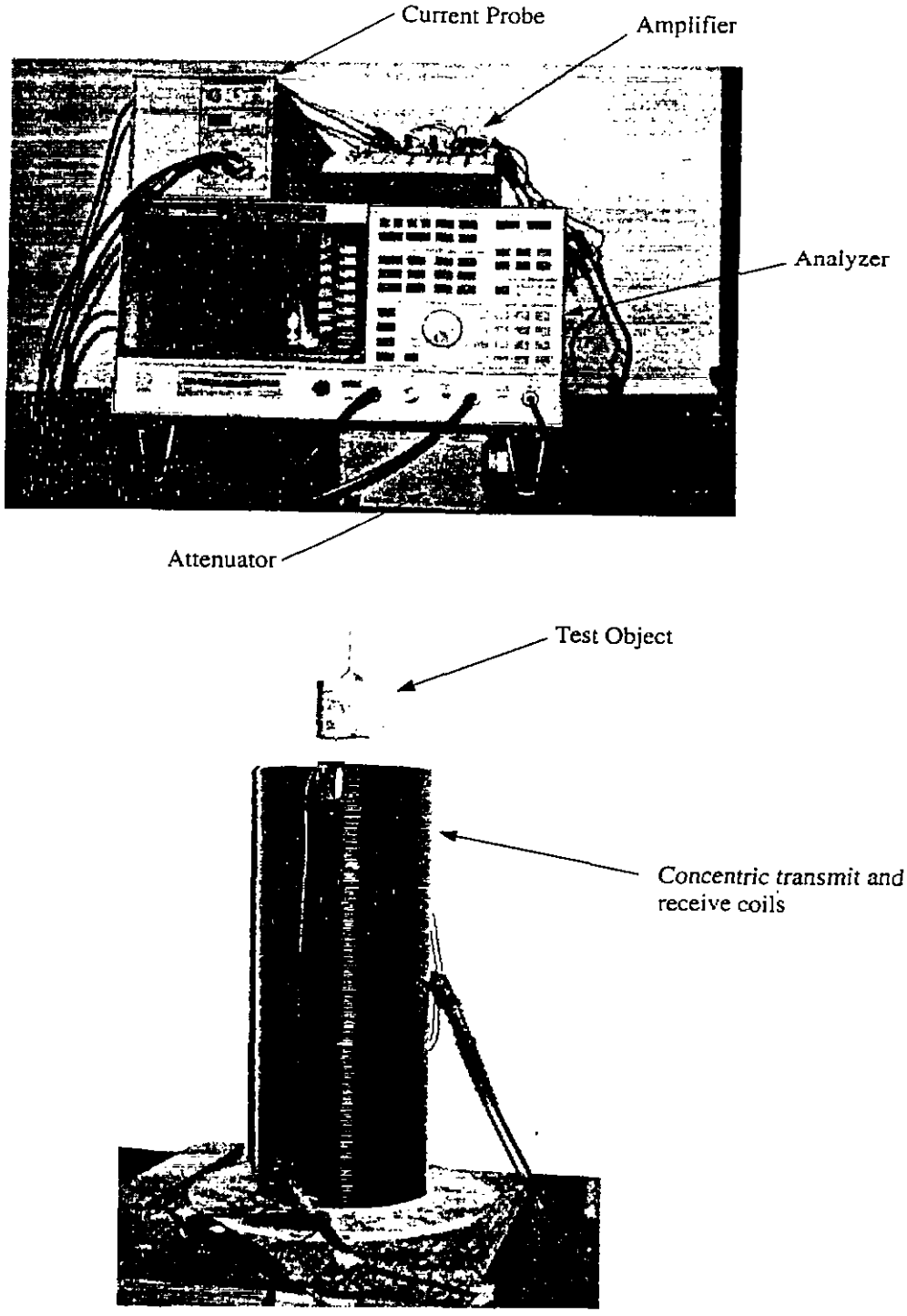

Figure 2.1. The equipment used in the experimental setup.

clockwise and counterclockwise turns making up what is sometimes referred to as a "bucking coil". As long as perfect symmetry is maintained, no voltage will exist at the output of the receive coil since the voltage induced across the clockwise turns will be of equal magnitude but opposite sign to that induced across the counterclockwise turns. As shown in Figure 2.2, a sample of the excitatory current measured by the current probe is applied to Channel One of the analyzer, whereas the output of the receive coil is applied to the input of the buffer amplifier. Finally, the output of the buffer amplifier connects to Channel Two of the analyzer. (The buffer amplifier is operated at unity gain and is used to present a large input impedance to the sensing coil.) Recall that the receive voltage is zero under symmetric conditions. Symmetry is broken by an object placed in the receive coil. The object's transfer function may be obtained by programming the analyzer to compute the ratio of the signal at Channel Two to the signal at Channel One at discrete frequencies over the band of interest.

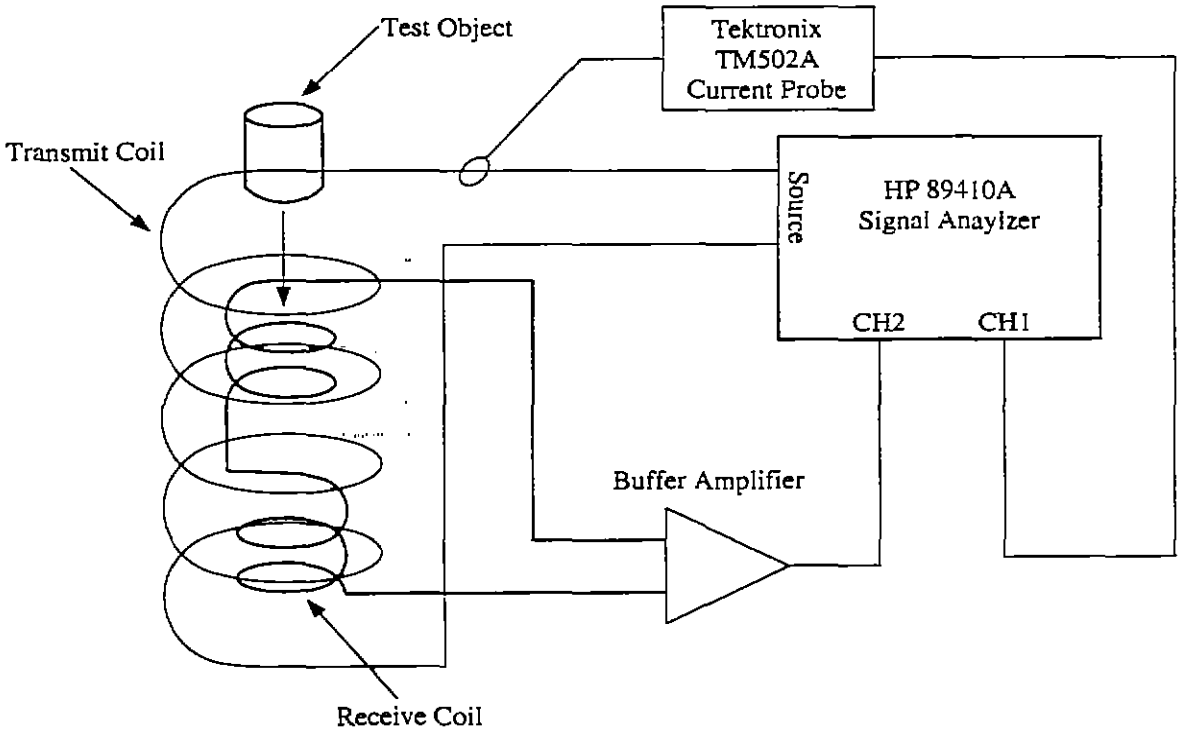

Figure 2.2. Block diagram of the experimental setup.

It is a simple matter to demonstrate that the experimental setup just described provides a means of determining the quasi-magnetostatic transfer function of a metallic object. For simplicity, take a simple short-circuited wire loop as the object of interest. A straightforward extension of the loop result, to be presented later, gives the desired general solution for an arbitrary finitely conducting metallic object. First, by Faraday's law, the voltage induced around the loop will be proportional to the time rate of change of

the magnetic flux passing through the loop (assume that the magnetic flux density vector and loop axis are aligned). The magnetic flux produced by the excitatory coil is in turn proportional to the excitatory current so one may write

$$V_{Object}(j\omega) \propto j\omega I_{Source}(j\omega) \tag{2.1}$$

with time differentiation replaced by multiplication by $j\omega$ (ω = radian frequency of oscillation = $2\pi f$.) At low frequencies, the quasi-magnetostatic approximation allows one to model the loop as a lumped parameter circuit consisting of a resistance R in series with an inductance L leading to a loop impedance

$$Z_{Object}(j\omega) = R + j\omega L \tag{2.2}$$

Loop current and voltage are related by

$$I_{Object}(j\omega) \propto \frac{V_{Object}(j\omega)}{Z_{Object}(j\omega)} = \frac{j\omega I_{Source}(j\omega)}{Z_{Object}(j\omega)} \tag{2.3}$$

Loop currents give rise to a "scattered" magnetic field which in turn induces a voltage in the receive coil, again in accordance with Faraday's Law as in (2.1)

$$V_{Receive}(j\omega) \propto j\omega I_{Object}(j\omega) = \frac{(j\omega)(j\omega) I_{Source}(j\omega)}{Z_{Object}(j\omega)}$$

or

$$H(j\omega) = \text{Loop Transfer Function} \propto \frac{V_{Receive}(j\omega)}{j\omega I_{Source}(j\omega)} = \frac{V_{Receive}(j\omega)}{V_{Object}(j\omega)} = \frac{j\omega}{Z_{Object}(j\omega)} \tag{2.4}$$

Clearly, the ratio (2.4) depends only on frequency and loop equivalent circuit elements (resistance R and inductance L) and may therefore be considered the transfer function of the loop.

Substituting (2.2) into (2.4) and performing a few steps of algebra leads to

$$H(j\omega) = \frac{\alpha^2}{1+\alpha^2} + j\frac{\alpha}{1+\alpha^2} \tag{2.5}$$

with $\alpha = \omega L/R = \omega\tau$. As shown in Figure 2.3 and in accordance with (2.5), the loop transfer function is high pass, so as the dimensionless parameter α increases (increasing frequency) the real part of the transfer function approaches unity while the imaginary part approaches zero as $1/\alpha$. Real and imaginary parts of the loop transfer function are equal at the crossover frequency where $\alpha = 1$ or

$$f_{crossover} = \frac{1}{2\pi\tau} = \frac{R}{2\pi L}. \tag{2.6}$$

At the crossover frequency the transfer function phase is equal to 45° and its magnitude is approximately 3 dB below its asymptotic value. As a practical matter, the object's response is difficult to measure at low

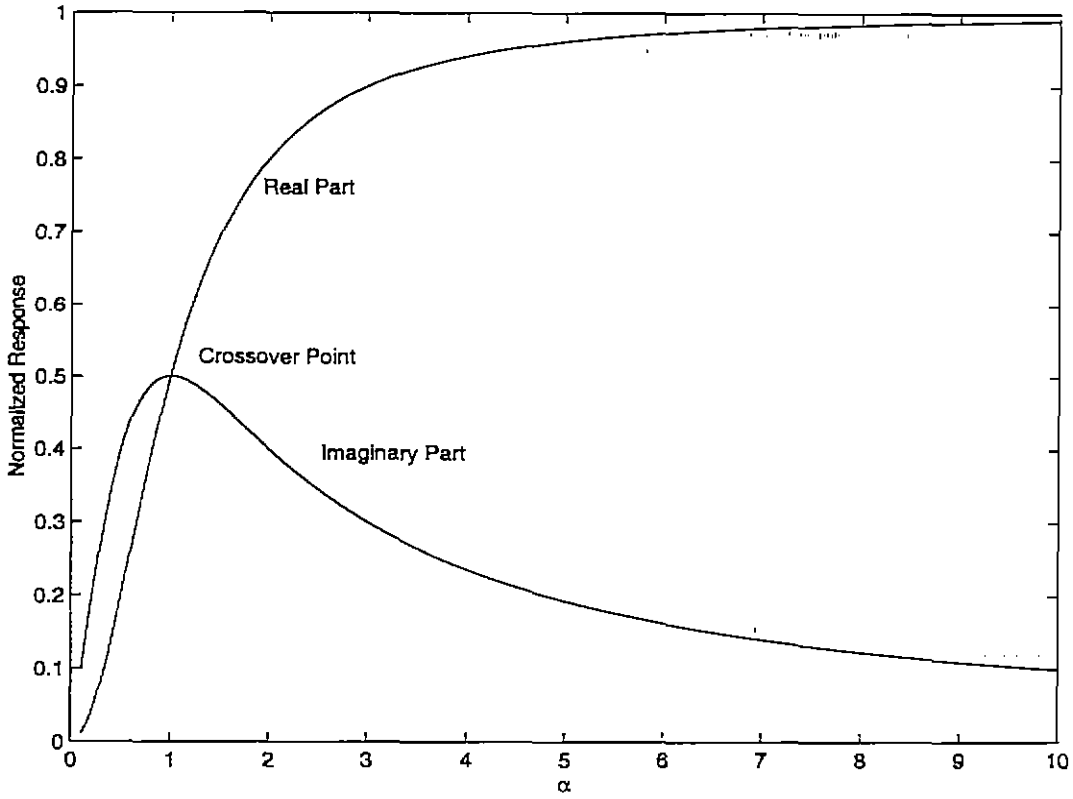

Figure 2.3. The response of a metallic object by a low-frequency magnetic field as given by (2.5).

frequencies since the transfer function approaches $-\infty$ dB as f approaches zero and noise will compromise the fidelity of the measurement. One can improve the quality of the measurement by averaging, but there is a practical limit here too since many averages at very low frequencies requires a substantial amount of time.

Sower [4] has shown that the time constant of the loop, τ, is proportional to the square of the wire radius (and to the conductivity) and varies only slightly with loop size whereas the the amplitude of the loop response varies with the cube of the loop radius and varies only slightly with wire radius. It therefore becomes possible, at least to first order, to independently adjust the crossover frequency and amplitude of the loop response. Taking advantage of this feature, one may approximate the response of an arbitrary metallic object with a simple wire loop opening up the possibility of developing mine decoys (or simulants). As another application, a family of wire loops might be constructed so as to uniformly stress metal detectors. At one extreme, a loop of large radius constructed of low gauge wire would be very easy to detect. At the other extreme, a small radius loop made of a thin, high-gauge wire would be extremely difficult to detect.

Sower [4] shows that a pair of coaxial loops has a transfer function consisting of two terms like that

of (2.5) above with

$$\tau_1 = \frac{L_1 + M}{R_1} \qquad \tau_2 = \frac{L_2 + M}{R_2} \tag{2.7}$$

where R_1, R_2 and L_1, L_2 are the resistance and inductance of loops 1 and 2, respectively, and M is the mutual inductance between the loops. Arbitrary bodies can be viewed as being made up of a number of loops of different size resulting, in general, in a infinite number of terms as in (2.5) each with a different amplitude. Therefore, our final model for the objects of interest here becomes

$$Y(j\omega) = \sum_{i=1}^{N} j\omega \left[\frac{a_i}{\sigma_i + j\omega}\right] + V(j\omega) \tag{2.8}$$

where a_i is the real valued coupling coefficient of the ith mode, σ_i is the pole term of the ith mode, and $V(j\omega)$ is additive white Gaussian noise which is an inevitable consequence of the measurement process.

Before moving on to the next section, we reiterate that the general form of the response presented above is correct only for non-permeable objects. Baum [1, 6] gives the step-function quasi-magnetostatic scattering polarizability dyadic as

$$\frac{1}{s} \overleftrightarrow{M}(s) = \frac{1}{s} \overleftrightarrow{M}(0) + \sum_{\alpha} \frac{M_\alpha}{s_\alpha} \vec{\mathrm{M}}_\alpha \vec{\mathrm{M}}_\alpha \left[s - s_\alpha\right]^{-1} \tag{2.9}$$

where $\overleftrightarrow{M}(0)$ is the D.C. magnetic polarizability term required to correctly represent the response of permeable objects. Alternatively, the δ-function response [1, 6] takes the form

$$\overleftrightarrow{M}(s) = \overleftrightarrow{M}(\infty) + \sum_{\alpha} \vec{\mathrm{M}}_\alpha \vec{\mathrm{M}}_\alpha \left[s - s_\alpha\right]^{-1} \tag{2.10}$$

with $\overleftrightarrow{M}(\infty)$ the magnetic-polarizability dyadic of a perfectly conducting target. Observe that by adding a constant term to (2.8) and multiplying this sum by frequency ($j\omega$), one obtains a scalar from of (2.9). Specifically,

$$Y(j\omega) = m(0) + \sum_{i=1}^{N} j\omega \left[\frac{a_i}{\sigma_i + j\omega}\right] + V(j\omega) \tag{2.11}$$

is just (2.8) corrected to account for non-permeable objects that have a finite D.C. response ($m(0)$).

For completeness, Figure 2.4 shows the response of a 2.5 inch diameter ferrous sphere. (The sphere was not used in our identification work.) Comparing Figures 2.3 and 2.4, the most notable difference is that the real part of the response for the ferrous sphere passes through zero and becomes negative below some frequency, referred to by some as the crossover frequency (not to be confused with the crossover frequency as defined above for non-permeable objects). At very low frequencies the imaginary part of the response approaches zero, just like with non-permeable objects, while the real part continues toward some finite

negative value. In the high frequency limit, the real/imaginary part of the permeable response approaches a finite value/zero in a manner identical to that for non-permeable objects. Sower [4] points out that the step response (time domain) of magnetic spheres has an initial fast rise from zero followed by a much slower decay back to zero. He suggests that the response can be modeled as a series of exponential decay terms, with the slower decay terms having coefficients of opposite sign to those of the faster terms. This model agrees with (2.11) above with some coupling coefficients positive and some negative. Using the knowledge that our test objects were all non-magnetic, made from either aluminum or copper, allowed us to assign a very low probability to competing models with negative coupling coefficients.

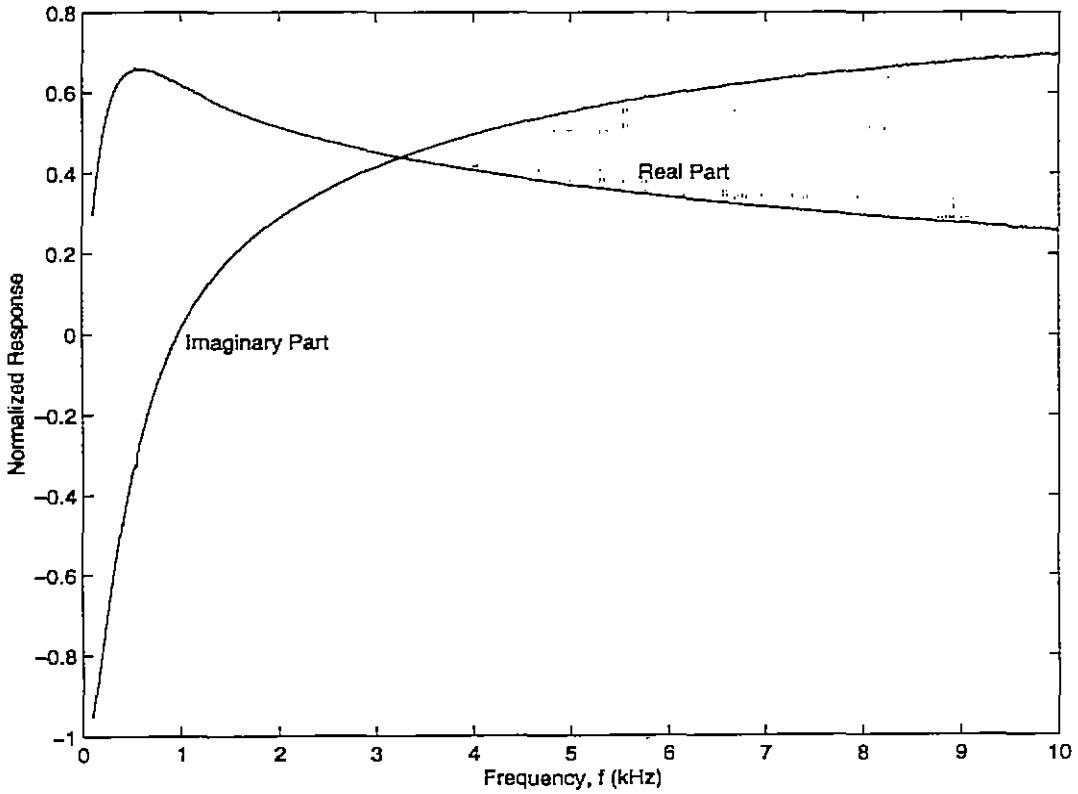

Figure 2.4. The low-frequency response of the ferrous sphere.

3. Pole Extraction

3.1 Introduction

Once the model for an object's response is known, the next step is to extract the model parameters from the measured data. This can present a challenge because the response contains only real poles which correspond to non-oscillatory exponential decays in the time domain. Without oscillation, a response containing multiple poles can be approximated reasonably well under certain conditions by a response with fewer poles. Furthermore, if the approximation error is sufficiently smaller than the noise in the measured data, then the lower order (approximated) response is sufficient to characterize the underlying model. For example, let the true response be a sum of two exponential decays in the time-domain,

$$f(t) = a_1 e^{\sigma_1 t} + a_2 e^{\rho\sigma_1 t} \tag{3.1}$$

where ρ is the ratio of the two poles. Let the approximated response be a single exponential decay,

$$f_{app}(t) = a_{app} e^{\sigma_{app} t} \tag{3.2}$$

where

$$a_{app} \approx a_1 + a_2 \quad and \quad \sigma_{app} \approx \sigma_1 \ln\left(\frac{a_1 e^{-1} + a_2 e^{-\rho}}{a_{app}}\right)$$

The measured response $z(t)$ in the presence of noise $v(t)$ can be written as

$$z(t) = f(t) + v(t) \tag{3.3}$$

$$= f_{app}(t) + e(t) + v(t) \tag{3.4}$$

where, $e(t) = f(t) - f_{app}(t)$, is the approximation error. For $a_1 = a_2 = 0.5$, the maximum value of this error is plotted versus ρ in Figure 3.1. Experimentally, it was found that when the maximum error is less than the standard deviation of the noise, the methods described in the next section could not identify the two original poles but could only extract the pole from the approximated response. For an SNR of 30dB, the allowable standard deviation for the noise is about 0.01. Thus, as shown in Figure 3.1 for this SNR, a pole ratio (ρ) less than about 1.75 will cause the pole extraction algorithm to return the approximate pole instead of the two original poles. This occurrence is even more pronounced when more poles are present. As a second example, let the true response be a sum of six equally weighted decays

$$f(t) = \frac{1}{6}e^{-100t} + \frac{1}{6}e^{-500t} + \frac{1}{6}e^{-1000t} + \frac{1}{6}e^{-5000t} + \frac{1}{6}e^{-10000t} + \frac{1}{6}e^{-20000t} \tag{3.5}$$

and the approximated response be a sum of three exponential decays

$$f_{app}(t) = a_1 e^{\sigma_1 t} + a_2 e^{\sigma_2 t} + a_3 e^{\sigma_3 t} \tag{3.6}$$

Using the Differential Corrections method described in section 3.2.3, the parameters for the approximated response are found to be $a_1 = 0.180$, $a_2 = 0.327$, $a_3 = 0.468$, $\sigma_1 = -104.5$, $\sigma_2 = -739.3$, and $\sigma_3 = -9177.0$. The true response is plotted in Figure 3.2, and the approximation error is plotted in Figure 3.3. Note that the maximum error is around 0.01, implying that the noise standard deviation must be less than 0.01 to extract the original poles. Otherwise, the approximated response is sufficient to characterize the true underlying model. Experimentally, it was found that only two or three poles can be extracted from measured data even when more poles are present. Hence, when more than three poles are present in the measured data, the extracted poles are best thought of as characteristic values that reproduce the object's response rather than the actual poles of the system. These results apply to both time-domain and frequency-domain data.

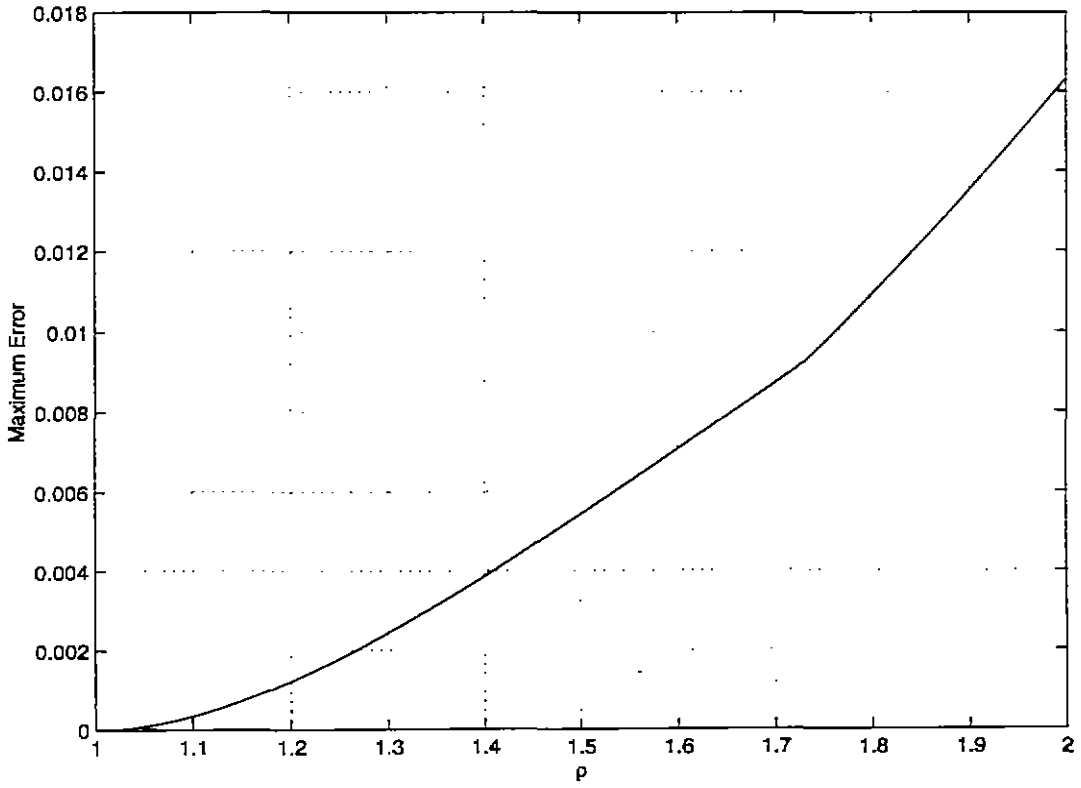

Figure 3.1. Maximum approximation error versus ρ.

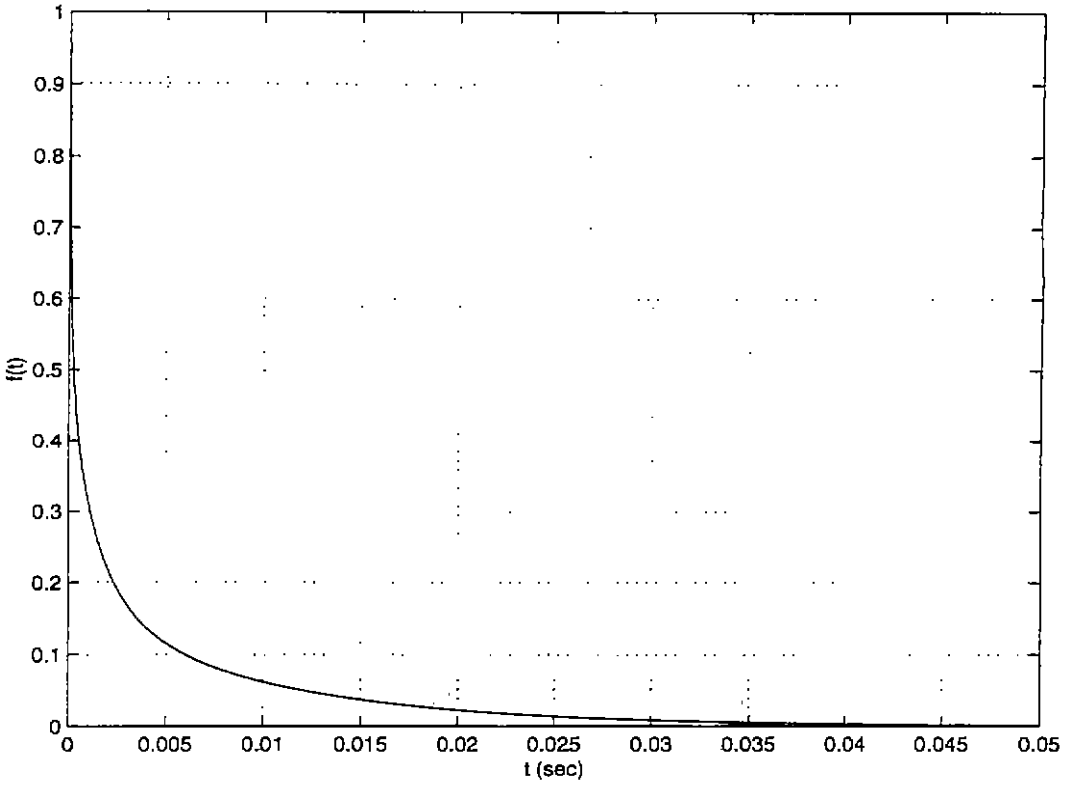

Figure 3.2. True six pole response.

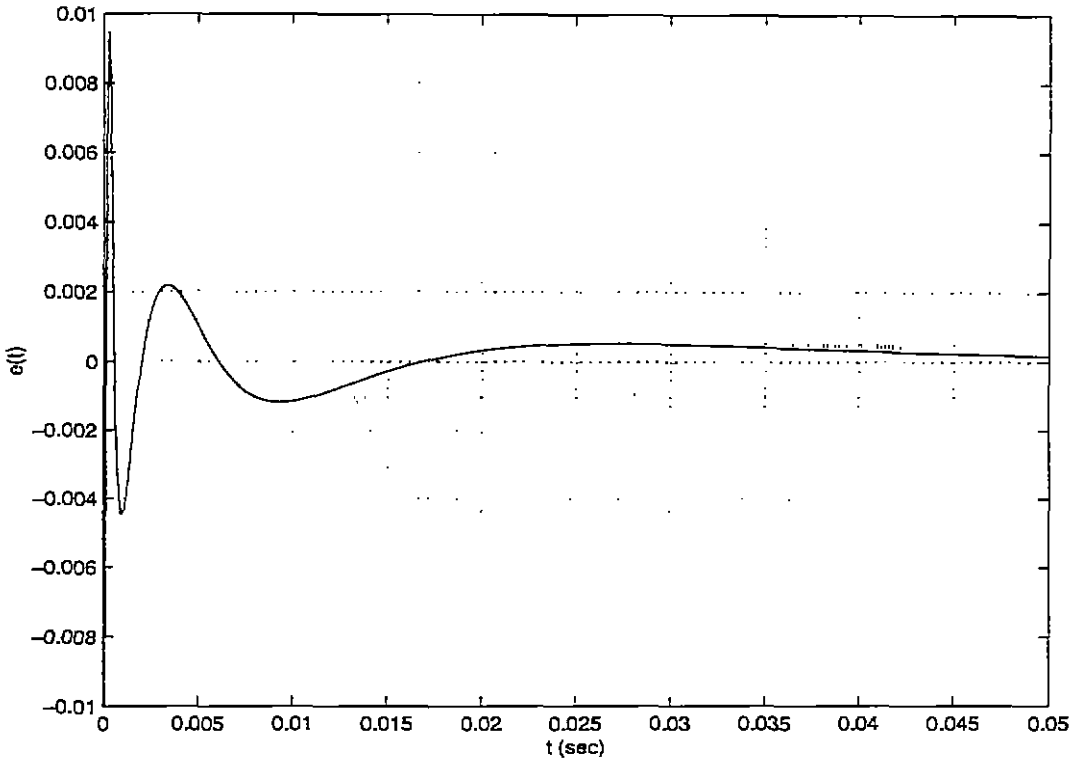

Figure 3.3. Approximation error for three pole approximation.

3.2 Methods for Pole Extraction

Several methods of extracting characteristic values, or poles, from measured data were evaluated including Prony's method, Matrix Pencil Method, Differential Corrections, and a Genetic Algorithm. The first two are time-domain methods, while the latter two can be used on time-domain or frequency-domain data. The following is a summary of each approach.

3.2.1 Prony Method

Given a time-domain impulse response of an object in the late-time, Prony's method can be used to determine the parameters of the exponential model [11]. Since the continuous time signal must be sampled, the discrete-time exponential model becomes

$$y(n) = \sum_{k=1}^{N} a_k z_k^n \quad with \quad z_k \equiv e^{s_k \Delta t} \tag{3.7}$$

Recognize that the discrete-time model is a solution to the following homogeneous difference equation whose roots are equal to the poles of the discrete-time model in (3.7),

$$\sum_{k=0}^{N} x_{N-k} y(n-k) = 0, \quad x_N = 1 \tag{3.8}$$

Since the data is given, this equation represents a system of equations that can be solved for x_k's. Finally, the pole locations are estimated as the roots of the following polynomial,

$$X(z) = \sum_{k=0}^{N} x_k z^k \tag{3.9}$$

Note that this procedure is applicable to frequency domain data through Fourier Transform techniques. Due to the inherent noise in measured data, the x_k's solved for in (3.9) will not be exact. Furthermore, small perturbations in the x_k's can produce large perturbations in the root locations which implies that this method of extracting poles from measured data is highly sensitive to noise. An improved Prony method for extracting poles, called the Total Least Squares (TLS) Prony method, accounts for noise in the data and provides better performance than the traditional Prony method [12]. However, the most significant factor limiting the performance of the Prony method is the lack of structure in the data. When more than two poles are present in the data, the Prony method occasionally returns poles that are unreasonable from a physical standpoint, such as unstable or complex poles. Due to this performance deficiency along with the fact that the Prony method is not a direct frequency-domain method, other methods were found to have better performance on frequency-domain data with real poles.

3.2.2 Matrix Pencil

Similar to the Prony method, the Matrix Pencil method assumes the measured data to be of the form given in (3.7), and the poles are found by solving a generalized eigenvalue problem. One advantage this method has over the Prony method is that an estimate of the number of poles can be obtained by performing a singular value decomposition on the data matrix defined in [13]. The number of poles, N, in the data is determined by the number of singular values above a given threshold. See [13] for further details on this approach. As with the Prony method, the Matrix Pencil method performs poorly when the data contains multiple, real poles. Furthermore, this method is a time-domain method and is not directly applicable to frequency-domain data.

3.2.3 Differential Corrections

Since the model for the frequency domain data is known, the Differential Corrections technique is an iterative method which performs a nonlinear least squares fit of the data to the model in order to extract model parameters [14]. To simplify exposition, assume a frequency-domain model with two distinct poles, σ_1 and σ_2.

$$F(a_1, a_2, \sigma_1, \sigma_2, \omega) = a_1 \frac{j\omega}{\sigma_1 + j\omega} + a_2 \frac{j\omega}{\sigma_2 + j\omega} \tag{3.10}$$

With initial estimates of the model parameters given, improved estimates are obtained by increments, $a_{k(new)} = a_{k(old)} + \Delta a_k$ *and* $\sigma_{k(new)} = \sigma_{k(old)} + \Delta\sigma_k$. Expanding the model in a Taylor series about the initial parameter estimates and neglecting higher order derivatives gives,

$$F = F(a_{k(old)}, \sigma_{k(old)}, \omega) + \left(\frac{\partial F}{\partial a_1}\right)_{old} \Delta a_1 + \left(\frac{\partial F}{\partial a_2}\right)_{old} \Delta a_2 + \left(\frac{\partial F}{\partial \sigma_1}\right)_{old} \Delta\sigma_1 + \left(\frac{\partial F}{\partial \sigma_2}\right)_{old} \Delta\sigma_2 \tag{3.11}$$

where the subscript "old" indicates that the expression is evaluated at the old parameter estimates. To improve the parameter estimates, the following error function is minimized:

$$error = \sum_i \left([\mathrm{Re}(z_i) - \mathrm{Re}(F_i)]^2 + [\mathrm{Im}(z_i) - \mathrm{Im}(F_i)]^2 \right) \tag{3.12}$$

where z_i are measurements at ω_i, and F_i is the new fit function at ω_i. As will be discussed in section 3.3, the parameters that minimize this error function are the maximum likelihood parameter estimates when the noise has a Gaussian distribution. Minimizing the error requires that

$$\frac{\partial(error)}{\partial a_1} = 0, \quad \frac{\partial(error)}{\partial a_2} = 0, \quad \frac{\partial(error)}{\partial \sigma_1} = 0, \text{ and } \frac{\partial(error)}{\partial \sigma_2} = 0.$$

Expanding the first condition leads to

$$\frac{\partial}{\partial a_1}\sum_i \left([\mathrm{Re}(z_i)-\mathrm{Re}(F_i)]^2+[\mathrm{Im}(z_i)-\mathrm{Im}(F_i)]^2\right)=0$$

$$\sum_i \left(2[\mathrm{Re}(z_i)-\mathrm{Re}(F_i)]\left[-\frac{\partial \mathrm{Re}(F_i)}{\partial a_1}\right]+2[\mathrm{Im}(z_i)-\mathrm{Im}(F_i)]\left[-\frac{\partial \mathrm{Im}(F_i)}{\partial a_1}\right]\right)=0$$

Substituting (3.11) for the first and third F_i in the above expression and simplifying gives one equation with four unknowns (Δa_1,Δa_2,$\Delta\sigma_1$,$\Delta\sigma_2$),

$$A_{11}\Delta a_1+A_{12}\Delta a_2+A_{13}\Delta\sigma_1+A_{14}\Delta\sigma_2=B_1 \tag{3.13}$$

Expanding the partial derivatives with respect to the other parameters will give four equations and four unknowns that can be organized in matrix form as

$$\begin{bmatrix} A_{11} & A_{12} & A_{13} & A_{14} \\ A_{21} & A_{22} & A_{23} & A_{24} \\ A_{31} & A_{32} & A_{33} & A_{34} \\ A_{41} & A_{42} & A_{43} & A_{44} \end{bmatrix}\begin{bmatrix} \Delta a_1 \\ \Delta a_2 \\ \Delta\sigma_1 \\ \Delta\sigma_2 \end{bmatrix}=\begin{bmatrix} B_1 \\ B_2 \\ B_3 \\ B_4 \end{bmatrix} \tag{3.14}$$

where

$$A_{jk}=\sum_i\left[\frac{\partial \mathrm{Re}(F_i)}{\partial a_j}\frac{\partial \mathrm{Re}(F_i)}{\partial a_k}+\frac{\partial \mathrm{Im}(F_i)}{\partial a_j}\frac{\partial \mathrm{Im}(F_i)}{\partial a_k}\right] \quad for\ \ j=1,2\ and\ k=1,2$$

$$A_{jk}=\sum_i\left[\frac{\partial \mathrm{Re}(F_i)}{\partial a_j}\frac{\partial \mathrm{Re}(F_i)}{\partial \sigma_{k-2}}+\frac{\partial \mathrm{Im}(F_i)}{\partial a_j}\frac{\partial \mathrm{Im}(F_i)}{\partial \sigma_{k-2}}\right] \quad for\ \ j=1,2\ and\ k=3,4$$

$$A_{jk}=\sum_i\left[\frac{\partial \mathrm{Re}(F_i)}{\partial \sigma_{j-2}}\frac{\partial \mathrm{Re}(F_i)}{\partial a_k}+\frac{\partial \mathrm{Im}(F_i)}{\partial \sigma_{j-2}}\frac{\partial \mathrm{Im}(F_i)}{\partial a_k}\right] \quad for\ \ j=3,4\ and\ k=1,2$$

$$A_{jk}=\sum_i\left[\frac{\partial \mathrm{Re}(F_i)}{\partial \sigma_{j-2}}\frac{\partial \mathrm{Re}(F_i)}{\partial \sigma_{k-2}}+\frac{\partial \mathrm{Im}(F_i)}{\partial \sigma_{j-2}}\frac{\partial \mathrm{Im}(F_i)}{\partial \sigma_{k-2}}\right] \quad for\ \ j=3,4\ and\ k=3,4$$

$$B_j=\sum_i\left([\mathrm{Re}(z_i)-\mathrm{Re}(F_{old})]\frac{\partial \mathrm{Re}(F_i)}{\partial a_j}+[\mathrm{Im}(z_i)-\mathrm{Im}(F_{old})]\frac{\partial \mathrm{Im}(F_i)}{\partial a_j}\right) \quad for\ \ j=1,2$$

$$B_j=\sum_i\left([\mathrm{Re}(z_i)-\mathrm{Re}(F_{old})]\frac{\partial \mathrm{Re}(F_i)}{\partial \sigma_{j-2}}+[\mathrm{Im}(z_i)-\mathrm{Im}(F_{old})]\frac{\partial \mathrm{Im}(F_i)}{\partial \sigma_{j-2}}\right) \quad for\ \ j=3,4$$

Solving this system of equations for the "differential" parameters and adding them to the previous estimates will give better estimates of the parameters. After several iterations, the parameters should converge. Note that this method requires initial guesses of the parameters, including the number of poles N. When the number of poles in the model exceeds the actual number of poles in the data (or the number of poles required to reconstruct the data), the parameters do not converge because the equations in (3.14) are no

longer linearly independent. This method converges rapidly and works on time or frequency-domain data with non-uniformly sampled data points. As with any gradient search scheme, the shortcoming of this approach is that the converged parameters do not necessarily represent the global minimum of the error function defined in (3.12). Consequently, this method can be used in conjunction with the Genetic Algorithm described next to verify that the parameters from a given data set represent a global minimum of the error function.

3.2.4 Genetic Algorithm

The Genetic Algorithm approach is patterned after the natural processes of genetic evolution and survival of the fittest to provide a global minimum of the error function defined in (3.12). The algorithm encodes each parameter into a binary sequence, called a gene, and a set of genes defines a chromosome. The chromosomes undergo natural selection, mating, competition, and mutation to arrive at the optimal solution. Details of this approach along with Matlab code to implement a genetic algorithm are given in [15]. A drawback of this approach is the typically slow convergence of the parameters. Furthermore, since the parameters must be discretized, more accurate representation of the parameters requires longer chromosome lengths which further increases computation time. Despite these drawbacks, the Genetic Algorithm was used successfully to verify the results given by the Differential Corrections method and, in some cases, to provide initial guesses of parameters for the Differential Corrections method.

3.3 Statistical Analysis of Pole Extraction Methods

Of the methods mentioned in the previous section, the Differential Corrections method in conjunction with the Genetic Algorithm were used to extract poles from measured frequency-domain data. Before these results can be presented, however, justification of the error function defined in (3.12) and the variance of the extracted parameters must be addressed. A desirable estimator for the model parameters of (3.10) is one that provides an efficient estimate, achieving the Cramér-Rao (CR) lower bound [21]. If such an estimator exists, then it is the maximum likelihood estimate (MLE) and can be obtained by minimizing the log-likelihood function,

$$\left.\frac{\partial \ln p(\mathbf{Z}|\Theta)}{\partial \theta_j}\right|_{\theta_j=\hat{\theta}_{j_{ml}}} = 0 \quad for\ j = 1, \ldots, n \tag{3.15}$$

where $\mathbf{Z} = [z_1, z_2, \ldots, z_L]$ is the measured data vector and $\Theta = [\theta_1, \ldots, \theta_n]$ is the parameter vector. The measured data can be expressed as the model plus noise, v_i

$$z_i = F(\theta_1, \ldots, \theta_n, \omega_i) + v_i = F_i + v_i \tag{3.16}$$

Since a statistical characterization of all the noise sources is not known, and for mathematical tractability, the noise is assumed to be (complex) white Gaussian noise with zero mean and variance σ_v^2. With this

assumption the likelihood function can be written [18],

$$p(\mathbf{Z}|\Theta) = \prod_{i=1}^{L} \left(\frac{1}{\pi\sigma_v^2} \exp\left[-\frac{|z_i - F_i|^2}{\sigma_v^2} \right] \right) \tag{3.17}$$

and the log-likelihood function becomes

$$\ln p(\mathbf{Z}|\Theta) = L \ln\left(\frac{1}{\pi\sigma_v^2}\right) - \frac{1}{\sigma_v^2} \sum_{i=1}^{L} \left(|z_i - F_i|^2\right) \tag{3.18}$$

Minimizing this expression with respect to each parameter gives the maximum likelihood estimates.

$$\frac{\partial\left(\sum_{i=1}^{L} |z_i - F_i|^2\right)}{\partial\theta_j} = 0 \quad for \;\; j = 1, \ldots, n \tag{3.19}$$

Note that this is equivalent to minimizing the error function defined in (3.12) with respect to each parameter. Thus, with the additive white Gaussian noise assumption, finding the maximum likelihood estimate is equivalent to the nonlinear least squares solution [16].

The Cramér-Rao lower bound on the parameter estimates for the multiple-parameter case is given by

$$var\left(\hat{\theta}_i\right) \geq \psi_{ii} \tag{3.20}$$

where $\hat{\theta}_i$ is the ith parameter estimate and ψ_{ii} is the iith element of the n × n matrix $\Psi = \mathbf{J}^{-1}$, with $\mathbf{J}$ given by

$$J_{ij} = E\left[\frac{\partial \ln p(\mathbf{Z}|\Theta)}{\partial\theta_i} \frac{\partial \ln p(\mathbf{Z}|\Theta)}{\partial\theta_j} \right] \quad for \;\; i, j = 1, \ldots, n \tag{3.21}$$

The matrix $\mathbf{J}$ is referred to as the *Fisher information matrix* [21]. Note that this matrix, and thus the CR lower bound, depends on the parameter values, data length (L), and the noise variance (σ_v^2). The CR lower bound for several typical two and three pole models with generated noise, $\sigma_v^2 = 0.0001$ and $L = 1200$, were computed numerically and are shown in Table 3.1. Different noise variances will simply scale these results. Since a closed form solution does not exist for the ML parameter estimates, the variance of the estimates were found through 100 runs in a Monte Carlo simulation. The Differential Corrections method was used to extract model parameters (identical to those in Table 3.1) from generated noisy data. The variance of the extracted parameters using this method are given in Table 3.2. Since the variances are very close to the CR lower bound values, the ML estimate provides a *near* efficient estimate. The Monte Carlo simulation was repeated with a higher noise variance, $\sigma_v^2 = .01$, and produced similar results. It should be noted that the Prony Method does not coincide with the ML estimate in the presence of noise [16].

Model #	a_1	a_2	a_3	σ_1	σ_2	σ_3
1	0.6 (1.28e-5)	0.2 (8.26e-6)	0.2 (3.15e-6)	300 (7.18)	2000 (2.39e3)	12000 (1.34e4)
2	0.7 (4.87e-6)	0.2 (4.23e-6)	0.1 (4.19e-6)	500 (6.66)	4000 (6.62e3)	20000 (2.98e5)
3	0.8 (2.41e-6)	0.1 (2.17e-4)	0.1 (2.13e-4)	1000 (9.90)	10000 (7.47e5)	25000 (5.58e6)
4	0.7 (1.29e-6)	0.3 (8.96e-7)		2000 (26.0)	15000 (5.82e3)	
5	0.8 (4.60e-7)	0.2 (3.48e-7)		1500 (8.59)	20000 (1.87e4)	

Table 3.1. Cramér-Rao Lower bound for decaying exponential model parameters with $\sigma_v^2 = 0.0001$ and $L = 1200$. (Lower bound on variances are in parentheses)

Model #	a_1	a_2	a_3	σ_1	σ_2	σ_3
1	0.6 (1.43e-5)	0.2 (9.78e-6)	0.2 (3.23e-6)	300 (7.10)	2000 (2.40e3)	12000 (1.16e4)
2	0.7 (5.32e-6)	0.2 (4.55e-6)	0.1 (4.19e-6)	500 (6.66)	4000 (6.97e3)	20000 (2.95e5)
3	0.8 (2.48e-6)	0.1 (2.32e-4)	0.1 (2.27e-4)	1000 (11.2)	10000 (7.45e5)	25000 (6.32e6)
4	0.7 (1.33e-6)	0.3 (1.00e-6)		2000 (29.3)	15000 (5.55e3)	
5	0.8 (4.21e-7)	0.2 (3.98e-7)		1500 (8.28)	20000 (1.74e4)	

Table 3.2. Maximum Likelihood estimate variances for decaying exponential model parameters with $\sigma_v^2 = 0.0001$ and $L = 1200$. (Variances are given in parentheses)

3.4 Poles Extracted from Objects

Poles and residues (the σ_i and a_i of (3.10))for seven different objects were extracted using the Differential Corrections approach. The objects and their dimensions are listed in Table 3.3 and shown in Figure 3.4. Two or three poles were found for each object in each cardinal orientation as well as for arbitrary orientations. Before extracting the characteristic values from the objects, the data collected from the Vector Signal Analyzer was normalized by the largest data value to give residue values between 0 and 1. Table 3.4 contains the extracted poles with the associated residues for different orientations of each object. Note that most of the weight, or the largest residue value, lies in the lower order poles indicating that these poles are the most significant. As shown in Table 3.1, the lower order poles also have significantly smaller variances than the higher order poles. Figure 3.5 is a plot of the extracted poles without any residue information. The vertical axis corresponds to the value of the pole or characteristic value for the objects listed along the horizontal axis. Each 'x' marks the location of a pole. Each set of poles (indicated by a vertical dashed line) for a particular object represents a different orientation. For example, the aluminum block has three cardinal orientations given by the first three sets of poles followed by two sets of arbitrary orientations. Similarly, the square aluminum tube has only two cardinal orientations given by the first two sets of poles and is followed by a set of poles from an arbitrary orientation. Presentation of pole sets for the other objects follow this same pattern. An expanded view of the lower order (most significant) poles are also presented in Figure 3.5.

Note that the lowest order poles remain relatively constant for different orientations of an object, but differ from object to object. This result indicates that discrimination of different objects based on the object's lower order poles is possible. Note, as expected, that similar objects have similar poles. For example, the large aluminum cylinder and the aluminum cylinder that is 80% of the length of the large aluminum

cylinder (but with the same diameter) have almost identical poles. When different objects have similar poles, then as anticipated, discrimination becomes more difficult. The copper cylinder and the aluminum block have similar poles which indicates that these two objects might also be difficult to discriminate between. An object's dimensions, material properties, and orientation with respect to the excitation field influence its pole locations, so that a variation in dimension can be compensated for by a change in material properties or orientation to yield similar poles. Thus, a given set of poles do not necessarily represent a unique object. Nevertheless, most objects do have different pole locations and can be identified based on their low frequency response.

Object	*Dimensions*
Aluminum Block	1.5"H, 2"W, 2 7/16"L
Square Al. Tube	3"L, 1.5"W on ea. side, 0.125"thick
Aluminum Ring	1 3/16"L, 2.5"OD, 0.25"thick)
Al. Cyl. (Big)	1.5"dia., 2 5/8"L
Al. Cyl. (80% Big)	1.5"dia., 2"L
Al. Cyl. (Sm. Dia.)	7/8"dia., 2 5/8"L
Copper Cyl.	2 1/16"dia., 1 1/32"L

Table 3.3. Objects and Dimensions.

Object	*Orientation*	a_1	a_2	a_3	σ_1	σ_2	σ_3
Aluminum Block	Lg. Side Up	6.312e-01	1.950e-01	1.337e-01	3.184e+02	1.766e+03	1.265e+04
	Md. Side Up	6.481e-01	1.757e-01	1.335e-01	3.918e+02	2.210e+03	1.362e+04
	Sm. Side Up	6.511e-01	1.758e-01	1.334e-01	4.170e+02	2.424e+03	1.419e+04
	Arbitrary	6.256e-01	1.941e-01	1.367e-01	3.490e+02	1.905e+03	1.300e+04
	Arbitrary	6.292e-01	1.897e-01	1.385e-01	3.675e+02	1.994e+03	1.321e+04
Square Al. Tube	Parallel	8.676e-01	9.955e-02		1.066e+03	1.975e+04	
	Perpendicular	7.721e-01	8.465e-02	1.062e-01	1.028e+03	5.624e+03	2.181e+04
	Arbitrary	8.366e-01	6.390e-02	7.180e-02	1.108e+03	1.026e+04	2.772e+04
Aluminum Ring	Parallel	8.121e-01	1.439e-01		7.667e+02	1.280e+04	
	Perpendicular	6.920e-01	2.502e-01		1.925e+03	1.502e+04	
	Arbitrary	7.100e-01	1.393e-01	1.065e-01	8.469e+02	5.181e+03	2.141e+04
Al. Cyl. (Big)	Parallel	7.272e-01	1.582e-01	8.641e-02	5.749e+02	4.684e+03	2.347e+04
	Perpendicular	7.010e-01	1.777e-01	1.015e-01	5.531e+02	4.025e+03	2.183e+04
	Arbitrary	7.094e-01	1.672e-01	9.571e-02	5.735e+02	4.303e+03	2.226e+04
Al. Cyl. (80% Big)	Parallel	6.878e-01	1.731e-01	1.014e-01	6.118e+02	4.252e+03	2.101e+04
	Perpendicular	6.738e-01	1.876e-01	1.065e-01	5.837e+02	3.932e+03	2.105e+04
	Arbitrary	6.914e-01	1.814e-01	1.003e-01	6.246e+02	4.475e+03	2.292e+04
Al. Cyl. (Sm. Dia.)	Parallel	8.610e-01	2.356e-01		1.877e+03	2.544e+04	
	Perpendicular	8.066e-01	2.372e-01		1.485e+03	1.571e+04	
	Arbitrary	8.294e-01	2.296e-01		1.605e+03	1.839e+04	
Copper Cyl.	Parallel	6.621e-01	1.768e-01	1.152e-01	2.366e+02	1.380e+03	1.056e+04
	Perpendicular	7.075e-01	1.645e-01	9.364e-02	3.792e+02	2.988e+03	1.744e+04
	Arbitrary	6.766e-01	1.707e-01	1.113e-01	3.164e+02	2.004e+03	1.310e+04

Table 3.4. Extracted Poles (Note: Parallel/Perpendicular designations refer to the orientation of the cylinder's axis relative to that of the applied field.)

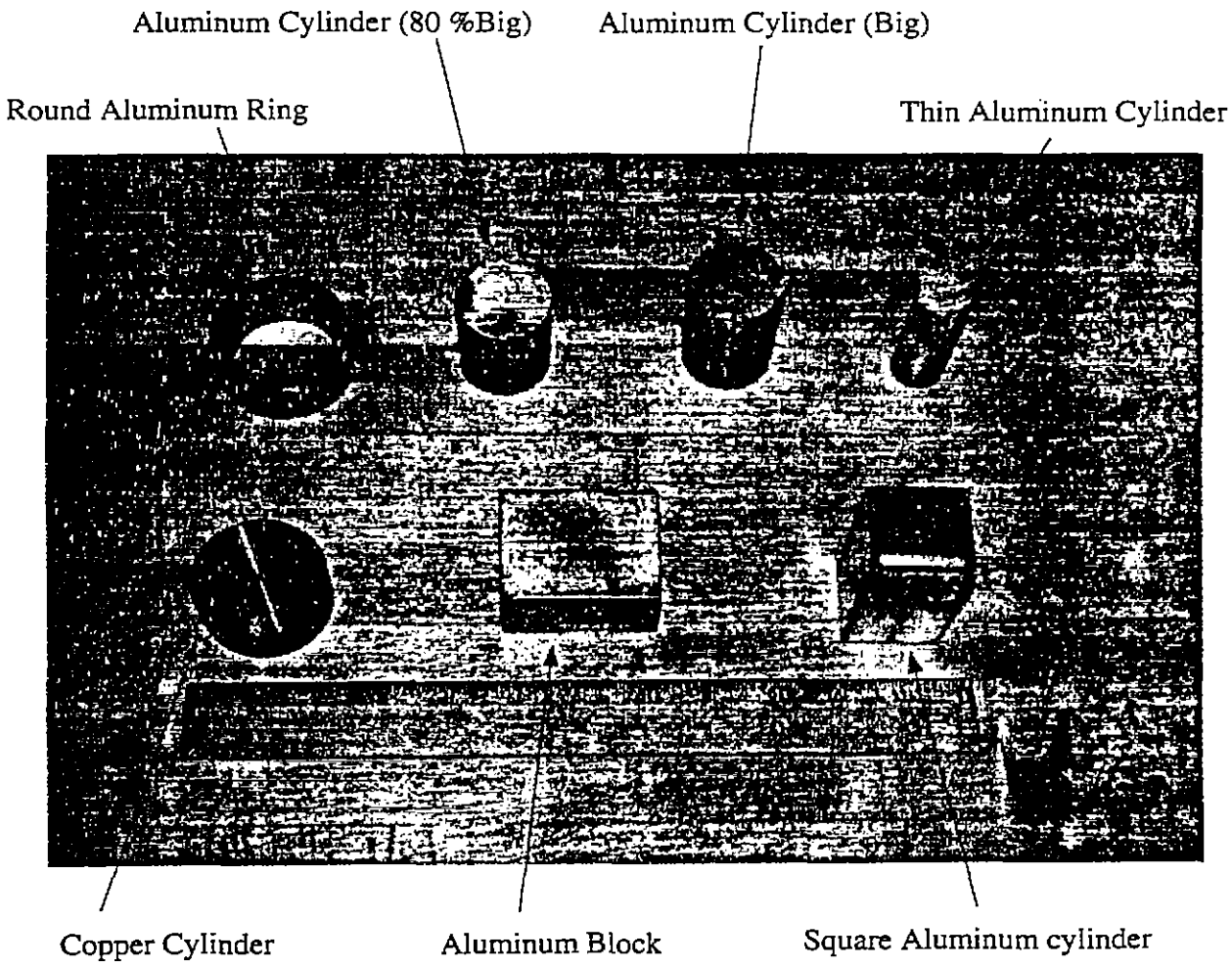
Aluminum Cylinder (80 %Big)
Aluminum Cylinder (Big)
Round Aluminum Ring
Thin Aluminum Cylinder
Copper Cylinder
Aluminum Block
Square Aluminum cylinder

Figure 3.4.

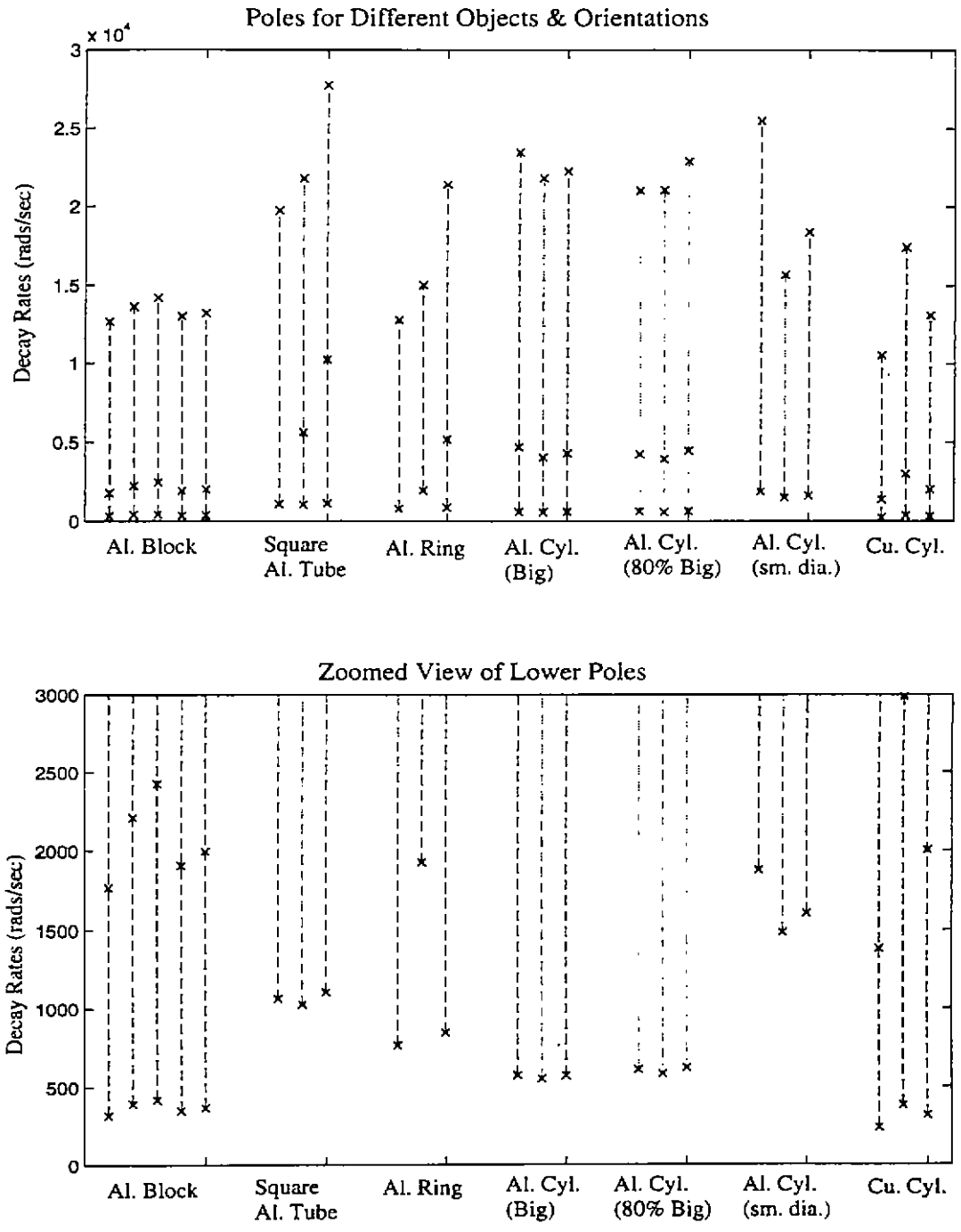

Figure 3.5. Pole Locations.

4. Identification Algorithm

The problem of interest here is to discriminate among a set of permeable, highly (but not perfectly) conducting objects using their low-frequency response. In order to simplify this problem, several assumptions are made. First, we assume that a target has been detected and that only a single target is responsible for the response. Furthermore, we assume that the target generating the return belongs to a group of targets for which we know a priori the poles (decay rates) of each. Based on these assumptions, we will develop a generalized likelihood ratio test (GLRT) to discriminate among a set of M known targets.

4.1 Problem Formulation

As mentioned previously, the concept of using a target's poles to perform target ID is based on the singularity expansion method (SEM) representation of the quasi-magnetostatic scattering from permeable and highly conducting scatterers [1]. Assuming a target exists and it's from a family of M possible candidates, then the SEM representation of the low-frequency response from the k-th target in the presence of noise can be written as

$$Y(j\omega) = \sum_{i=1}^{N} j\omega \left[\frac{a_i^{(k)}}{\sigma_i^{(k)} + j\omega} \right] + V(j\omega) \qquad 1 \le k \le M \tag{4.1}$$

where $a_i^{(k)}$ is the real valued coupling coefficient of the ith mode, $\sigma_i^{(k)}$ is the pole term of the ith mode, and $V(j\omega)$ is additive complex white Gaussian noise with zero mean and variance σ_v^2. The assumption that the noise is complex white Gaussian is reasonable for two reasons. First, it creates a mathematically tractable problem. Often, we will use a sub-optimal model for the randomness in the noise in order to obtain a final solution. Second, the assumption that the noise is white is reasonable unless there is strong evidence that it is highly correlated [18].

The signal model portion of equation (4.1) can be separated into its real and imaginary parts to yield

$$Y(j\omega) = \sum_{i=1}^{n} a_i^{(k)} \left[\frac{\omega^2}{(\sigma_i^{(k)})^2 + \omega^2} + j \frac{\omega \sigma_i^{(k)}}{(\sigma_i^{(k)})^2 + \omega^2} \right] + V(j\omega). \tag{4.2}$$

The purpose of separating the signal portion of (4.1) into its real and imaginary parts will be addressed later. Regardless of their form, equations (4.1) and (4.2) lead to the major question addressed in this section. That is, if we know a target belongs to a family of M targets, and we know the poles of the target, then what is the likelihood the target generated the return $Y(j\omega)$?

4.2 Algorithm Development

4.2.1 Discretization

For convenience as well as for practical implementation using DSP hardware, we denote the various signals in (4.2) by their samples:

$$\mathbf{Y} \equiv \begin{bmatrix} Y(j\omega_1) \\ Y(j\omega_2) \\ \vdots \\ Y(j\omega_q) \end{bmatrix}; \qquad \phi_i^k \equiv \begin{bmatrix} \phi_i^{(k)}(j\omega_1) \\ \phi_i^{(k)}(j\omega_2) \\ \vdots \\ \phi_i^{(k)}(j\omega_q) \end{bmatrix}; \qquad \psi_i^k \equiv \begin{bmatrix} \psi_i^{(k)}(j\omega_1) \\ \psi_i^{(k)}(j\omega_2) \\ \vdots \\ \psi_i^{(k)}(j\omega_q) \end{bmatrix}; \qquad \mathbf{V} \equiv \begin{bmatrix} V(j\omega_1) \\ V(j\omega_2) \\ \vdots \\ V(j\omega_q) \end{bmatrix}.$$

where

$$\phi_i^{(k)}(j\omega) = \frac{\omega^2}{(\sigma_i^{(k)})^2 + \omega^2} \qquad \psi_i^{(k)}(j\omega) = \frac{\omega\sigma_i^{(k)}}{(\sigma_i^{(k)})^2 + \omega^2} \tag{4.3}$$

and q is the total number of samples. Thus, the return signal vector $\mathbf{Y}$ under target k can be written in parametric form as

$$H_k: \qquad \mathbf{Y} = (\mathbf{\Phi}_k + j\mathbf{\Psi})\mathbf{A}_k + \mathbf{V} \tag{4.4}$$

where the unknown vector is

$$\mathbf{A}_k \equiv \begin{bmatrix} a_1^k \\ a_2^k \\ a_3^k \\ \vdots \\ a_N^k \end{bmatrix}_{(N\times 1)}$$

and the known signal modes are

$$\begin{aligned} \mathbf{\Phi}_k &= \begin{bmatrix} \phi_1^k & \phi_2^k & \cdots & \phi_N^k \end{bmatrix}_{(q\times N)} \\ \mathbf{\Psi}_k &= \begin{bmatrix} \psi_1^k & \psi_2^k & \cdots & \psi_N^k \end{bmatrix}_{(q\times N)}. \end{aligned}$$

For the analysis presented here, $\mathbf{A}_k$ is an unknown parameter vector in the identification of target k. The $\mathbf{A}_k$ are treated as unknown since in real applications, the coupling between the object and the source will vary due to object burial depth. The only known parameters are the poles and the frequency range of interest which determine $\mathbf{\Phi}_k$ and $\mathbf{\Psi}_k$, and the measured return $\mathbf{Y}$. Our task is to construct a robust detection method to determine which of the M known targets is most likely to generate the received noisy signal $\mathbf{Y}$ that depends on an unknown, but deterministic vector $\mathbf{A}$.

4.2.2 Hypothesis Testing

Having developed a model structure, it is now possible to apply hypothesis testing to generate a generalized likelihood ratio test (GLRT). However, before developing a GLRT, a brief review of the principles of hypothesis testing will be given. A complete discussion of this topic is provided in a number of textbooks including Van Trees [19], Poor [20], and Srinath [21]. Much of the discussion below parallels the discussion provided in Van Trees and Srinath.

The fundamental idea behind hypothesis testing is the following: given an observation or set of observations ($\mathbf{Y}$), develop a decision rule to decide among a set of alternatives (hypotheses) describing the observation(s). Almost always, these observations are imperfect. Hence, hypothesis testing addresses the issue of inference based on incomplete information and provides a mathematically rigorous approach to the target identification problem.

To simplify the discussion of hypothesis testing, consider the case in which only two mutually exclusive hypotheses exist, H_1 and H_2. In terms of the target identification problem, H_1 is viewed as the low frequency response of target 1 and H_2 as the low-frequency response of target 2. The essential components of the binary hypothesis problem are illustrated in Figure 4.1. The first component is a source whose output is either H_1 or H_2. The second and third components are the probabilistic transition mechanism and observation space, respectively. Depending on which hypothesis is true, the probabilistic transition mechanism maps the source output to the observation space according to some probability law. Generally, the probabilistic transition mechanism can be viewed as the component that distorts or corrupts the source output. When the distortion is random, probability theory can be applied to develop two conditional probability density functions (pdf): $p(\mathbf{Y}|H_1)$ and $p(\mathbf{Y}|H_2)$. (The notation $p(\mathbf{Y}|H_i)$ is read the probability of $\mathbf{Y}$ given that H_i is true.) Each point in the observation space is mapped according to these two density functions. The final aspect of the hypothesis testing problem is the decision rule which assigns each point in

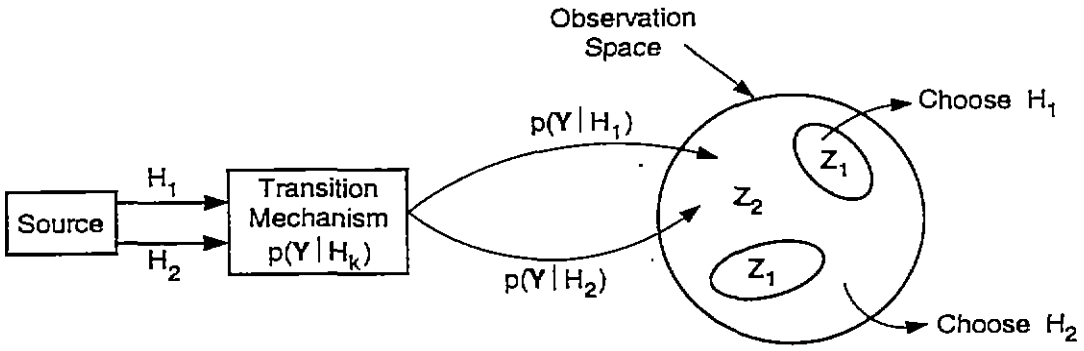

Figure 4.1. The fundamental aspects of a binary hypothesis testing problem.

the observation space to one of the hypotheses. The decision rule basically divides the observation space into two regions. If an observations falls in the region Z_1, hypothesis H_1 is chosen. Similarly, if an observation falls in the region Z_2, hypothesis H_2 is chosen.

One can think of a number of ways to develop a decision rule. However, a decision rule that is optimal in some sense would be preferred. To develop an optimal decision rule, all possible decisions must be considered. For the binary hypothesis problem, there are four possible outcomes:

- Choose H_1 when H_1 is true.
- Choose H_1 when H_2 is true.
- Choose H_2 when H_2 is true.
- Choose H_2 when H_1 is true.

Next, a cost is assigned to each outcome. The purpose of defining a cost is to assign some degree of importance to each outcome. The cost C_{ij} is the cost of making a decision D_i when hypothesis H_j is true. For example, C_{12} is the cost of choosing hypothesis H_1 when hypothesis H_2 is true.

To develop a decision rule, a Bayes criterion is applied. The Bayes criterion seeks to minimize the average cost. The average cost can be written as

$$\bar{C} = C_{11}P(D_1, H_1) + C_{12}P(D_1, H_2) + C_{21}P(D_2, H_1) + C_{22}P(D_2, H_2) \tag{4.5}$$

where $P(D_i, H_j)$ is the probability of deciding H_i and H_j is true. By applying Bayes Theorem, the average cost becomes

$$\bar{C} = C_{11}P(D_1|H_1)P(H_1) + C_{12}P(D_1|H_2)P(H_2) + C_{21}P(D_2|H_1)P(H_1) + C_{22}P(D_2|H_2)P(H_2). \tag{4.6}$$

The conditional probability $P(D_i|H_j)$ is determined by integrating the conditional probability density function $p(\mathbf{Y}|H_j)$ over the region Z_i. In doing so, the average cost becomes

$$\begin{aligned} \bar{C} \;=\; & C_{11}P(H_1)\int_{Z_1} p(\mathbf{Y}|H_1)\,d\mathbf{Y} + C_{12}P(H_2)\int_{Z_1} p(\mathbf{Y}|H_2)\,d\mathbf{Y} \\ & + C_{21}P(H_1)\int_{Z_2} p(\mathbf{Y}|H_1)\,d\mathbf{Y} + C_{22}P(H_2)\int_{Z_2} p(\mathbf{Y}|H_2)\,d\mathbf{Y}. \end{aligned} \tag{4.7}$$

The average cost is minimized by appropriately choosing the decision regions Z_1 and Z_2. Although not derived here (see Van Trees [19] for complete details), the appropriate choice of the decision regions leads to the following decision rule

$$\frac{p(\mathrm{y} \mid \text{target 1})}{p(\mathrm{y} \mid \text{target 2})} \underset{H_2}{\overset{H_1}{\gtrless}} \frac{P(H_1)(C_{21} - C_{11})}{P(H_2)(C_{12} - C_{22})} = \eta \tag{4.8}$$

Equation (4.8) is referred to as a likelihood ratio test (LRT). The right side of the LRT is known as the threshold η and is a function of the prior probabilities and the cost. If we assume that all targets are equally probable and when uniform cost (zero for a correct decision and one for an incorrect decision) is assumed, then the threshold is equal to one. If the left side of the LRT is greater than η, then we say hypothesis H_1 is true, or equivalently, target 1 is present. Similarly, if the ratio of the two likelihood functions is less than η, then target 2 is present. For multiple targets ($M > 2$), multiple LRT's need to be tested.

4.2.3 Generalized Hypothesis Testing

In order to apply the LRT to the problem of interest, the conditional probability density functions $p(\mathbf{Y}|H_i)$ must be defined. This can be done by considering the pdf of the noise $V(j\omega)$ in (4.4). Because the noise has been characterized as being white and Gaussian, the probability density function for $\mathbf{V}$ can be expressed as

$$p(\mathbf{V}) = \frac{1}{\pi^q \sigma_\nu^{2q}} \exp\left(-\frac{1}{2\sigma_\nu^2}\mathbf{V}^H\mathbf{V}\right) \tag{4.9}$$

where q represents the total number of samples and H denotes the Hermitian operator. If we know that target k is present, then the probability of getting $\mathbf{Y}$ is simply the probability that the noise $\mathbf{V}$ would make up the difference. Thus, by using (4.4), we can write the conditional probability density function of $\mathbf{Y}$ given target k as

$$p(\mathbf{Y} \mid \text{target } k) = \frac{1}{\pi^q \sigma_\nu^{2q}} \exp\left(-\frac{1}{2\sigma_\nu^2}\left[\mathbf{Y} - (\Phi_k + j\,\Psi_k)\,\mathbf{A}_k\right]^H\left[\mathbf{Y} - (\Phi_k + j\,\Psi_k)\,\mathbf{A}_k\right]\right). \tag{4.10}$$

The conditional probability density function in (4.10) is a function of the unknown parameter $\mathbf{A}_k$ and is often referred to as the likelihood function.

In order to use the LRT in (4.8) for the two-target case, the likelihood functions must be evaluated based on known $\Phi_k\mathbf{A}_k$ and $\Psi_k\mathbf{A}_k$. This in turn requires that we have complete knowledge of the noiseless signal. Although the LRT is a very useful tool in a number of applications, target identification can not benefit directly since orientation dependency results in an unknown parameter vector $\mathbf{A}_k$. In short, simple Bayesian hypothesis testing is not directly applicable to our problem.

One method of remedying this situation is to manipulate the LRT to see if the test does in fact depend on knowledge of $\mathbf{A}_1$ and $\mathbf{A}_2$. If the LRT does not depend on knowledge of $\mathbf{A}_1$ and $\mathbf{A}_2$, then the test is said to be uniformly most powerful (UMP) [19]. In this particular case, it can be shown that a UMP does not exist.

Since a UMP test does not exist, an alternative solution is to estimate $\mathbf{A}_1$ assuming target 1 is present, and then estimate $\mathbf{A}_2$ assuming target 2 is present. These estimates are then used in the LRT as if they were correct. If the maximum likelihood estimates are used, then the resulting LRT is referred to as a

generalized likelihood ratio test (GLRT) [19]. The GLRT can be written in a form similar to the LRT as

$$\text{GLRT}: \quad \frac{\max_{\mathbf{A}_1} p(\mathbf{Y} \mid \text{target 1})}{\max_{\mathbf{A}_2} p(\mathbf{Y} \mid \text{target 2})} \underset{H_2}{\overset{H_1}{\gtrless}} \eta \tag{4.11}$$

The maximum likelihood (ML) estimate $\hat{\mathbf{A}}_1$ is that value of $\mathbf{A}_1$ that maximizes the likelihood function $p(\mathbf{Y} \mid \text{target 1})$. According to Kay [22], "The rationale for this approach is that, because $\mathbf{Y}$ was observed, it must have been very likely. Hence, the value of $\hat{\mathbf{A}}_i$ that yields the largest probability for the observed value of $\mathbf{Y}$ is probably close to the true value." Once an ML estimate has been obtained, then $p(\mathbf{Y} \mid \text{target 1})$ is evaluated using $\hat{\mathbf{A}}_1$. An identical procedure is used to obtain the denominator of (4.11). The ML estimate is preferred because it is a very practical estimator and it is easy to implement. Furthermore, the ML estimator has the beneficial property of being efficient provided an efficient estimator exists. An efficient estimator is one that achieves the Cramér-Rao lower bound on mean square estimation error [19]. Thus, if an efficient estimator exists, the ML estimator will produce it [18].

To obtain an ML estimate, the likelihood function $p(\mathbf{Y} \mid \text{target } k)$ must be maximized under the assumption that target k is present. Maximizing the expression

$$\exp\left[-\frac{1}{\sigma_v^2}\left([\mathbf{Y} - (\mathbf{\Phi}_k + j\,\mathbf{\Psi}_k)\,\mathbf{A}_k]^H\,[\mathbf{Y} - (\mathbf{\Phi}_k + j\,\mathbf{\Psi}_k)\,\mathbf{A}_k]\right)\right]$$

is equivalent to minimizing $\| \mathbf{Y} - (\mathbf{\Phi}_k + j\,\mathbf{\Psi}_k)\,\mathbf{A}_k \|^2$, hence yielding a least squares solution to $\mathbf{Y} = (\mathbf{\Phi}_k + j\mathbf{\Psi}_k)\mathbf{A}_k$ as

$$\hat{\mathbf{A}}_{k,\max} = \left[\mathbf{\Phi}_k^T\mathbf{\Phi}_k + \mathbf{\Psi}_k^T\mathbf{\Psi}_k\right]^{-1}\left(\mathbf{\Phi}_k^T\,\text{Re}\{\mathbf{Y}\} + \mathbf{\Psi}_k^T\,\text{Im}\{\mathbf{Y}\}\right). \tag{4.12}$$

The estimate for the unknown parameter vector $\mathbf{A}_k$ is purely real. Since the $\mathbf{A}_k$ were defined to be real, the estimator was constrained to yield only real estimates. By separating the signal model into its real and imaginary parts in (4.2), we were able to develop an estimator to meet this constraint.

Substituting the least squares solution into the GLRT for the simple two target case (with $\eta = 1$) yields after some manipulation the decision rule

$$\| \mathbf{Y} - (\mathbf{\Phi}_1 + j\,\mathbf{\Psi}_1)\,\hat{\mathbf{A}}_{1,\max} \| \underset{H_1}{\overset{H_2}{\lessgtr}} \| \mathbf{Y} - (\mathbf{\Phi}_2 + j\,\mathbf{\Psi}_2)\,\hat{\mathbf{A}}_{2,\max} \|. \tag{4.13}$$

The test in (4.13) simply states that the estimate which produces the smallest error is chosen as the correct target. If we maintain the conditions of equal prior probabilities and uniform cost, then for multiple hypothesis testing, the above decision rule can be generalized for M target discrimination as

$$\text{decide } \{Y(j\omega)\} = \text{target } k \text{ if } \| \mathbf{Y} - (\mathbf{\Phi}_k + j\,\mathbf{\Psi}_k)\,\hat{\mathbf{A}}_{k,\max} \| \text{ is minimum.} \tag{4.14}$$

4.3 The Algorithm and the Pole Library

The structure of the identification algorithm is illustrated by the flow chart in Figure 4.2. As one can see, the structure of the algorithm is relatively simple and easy to implement. The heart of the program essentially involves repeated use of equations (4.12) and (4.14) for each target in the target library. As will be discussed in this section and section 4.5, the organization of the poles in the target library is a very critical aspect of the identification algorithm.

Before discussing the pole library, it is pertinent to describe the basic nature of the identification algorithm. Once a response Y has been retrieved from the HP89410A vector signal analyzer, the algorithm uses a maximum likelihood estimator (eq. (4.12)) to estimate the coupling coefficients based on knowledge of Y and the poles in the target library. Thus, if there are M targets in the library, M estimates of the coupling coefficients are made. The target whose poles produce the estimate that yields the best fit to the response Y is selected as the correct target. This statement is expressed mathematically in (4.14).

One simple and straightforward method of organizing the pole library for the targets described in the previous section is shown in Table 4.1. The poles for all orthogonal orientations of an object are stored under a single target description. This method of organizing the poles essentially ignores information about the orientation of the target. The major problem in structuring the library in this manner is that it gives

Target Description	Poles		
Large Aluminum Block	3.1843e+02	1.7668e+03	1.2659e+04
	3.9180e+02	2.2104e+03	1.3620e+04
	4.1706e+02	2.4240e+03	1.4198e+04
Square Aluminum Cylinder	1.0661e+03	1.9755e+04	1.0285e+03
	5.6243e+03	2.1813e+04	
Round Aluminum Ring	7.6673e+02	1.2807e+04	1.9256e+03
	1.5028e+04		
Large Aluminum Cylinder	5.7490e+02	4.6849e+03	2.3477e+04
	5.5311e+02	4.0257e+03	2.1834e+04
Small Aluminum Cylinder	6.1187e+02	4.2525e+03	2.1018e+04
	5.8373e+02	3.9326e+03	2.1053e+04
Thin Aluminum Cylinder	1.8771e+03	2.5441e+04	1.4849e+03
	1.5714e+04		
Copper Cylinder	2.3660e+02	1.3801e+03	1.0565e+04
	3.7929e+02	2.9885e+03	1.7441e+04

Table 4.1. One way of organizing the pole library.

too much freedom for the ML estimator. Through experimentation, it was discovered that given four or five poles from any one of the M targets, a response from any of the other targets could be "fitted" well. For the library shown in Table 4.1, each object contains a minimum of four poles. When all the discriminants (poles) fit the data well, this obviously creates problems with the identification process. The primary reason

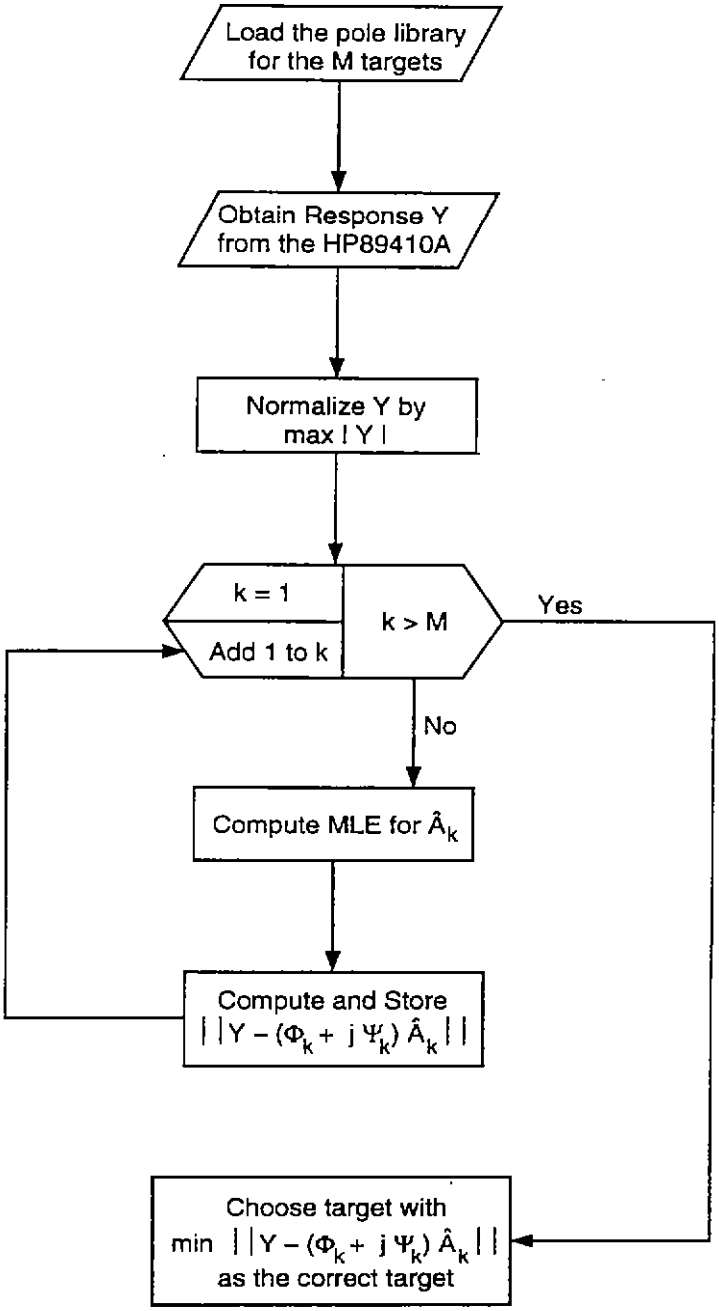

Figure 4.2. Flowchart for the identification algorithm.

why four or five poles will fit any response well is because of the nature of the responses under consideration. The low frequency responses from permeable, highly conducting objects contain very little structure, i.e. no zero crossings.

As an illustration, suppose the target library consists of the following two objects: the aluminum ring and the large aluminum cylinder. Furthermore, the pole library is arranged as described above and demonstrated in Table 4.1. Next, assume that the response $\mathbf{Y}$ is from the aluminum ring oriented with the open side of the ring perpendicular to the magnetic field. Figure 4.3 shows the real and imaginary parts of the low frequency response. Also, shown on Figure 4.3 is the real and imaginary parts of the estimated response which was obtained using the all the known poles of the aluminum ring. Figure 4.4 also shows the same response $\mathbf{Y}$, but the estimated response was obtained by using the poles of the large aluminum cylinder. Using (4.14), the error between the actual and estimated responses of Figure 4.3 is computed to be 0.0581. The error for the responses in Figure 4.4 is 0.0479. Thus, in this case, the wrong target (large aluminum cylinder) would have been selected as the correct target.

To improve performance, the pole library was rearranged to limit the freedom of the ML estimator. This was accomplished by organizing the pole library in terms of target description as well as orthogonal orientation. Table 4.2 displays this structure for the objects being studied in this report. Organizing the library by target description and orientation effectively treats each orthogonal orientation of an object as a different (or distinct) target. The obvious drawback to this method is that the size of the library more than doubles. However, as will be shown in the following section, the performance of the identification algorithm significantly improves. Furthermore, section 4.5 demonstrates that this method has superior performance on noisy data.

To demonstrate how the restructuring of the pole library improves performance, consider once again the two-target case considered earlier. Figure 4.5 shows the real and imaginary parts of the response $\mathbf{Y}$ from the aluminum ring oriented with its open side perpendicular to the magnetic field. Shown on the same figure is the estimated response which was found by using only the poles of the aluminum ring corresponding to the magnetic field perpendicular to the open side of the ring (row 6 of Table 4.2). Figure 4.6 shows the same response $\mathbf{Y}$, but the estimated response was obtained by using only the poles of the large aluminum cylinder corresponding to the perpendicular to end orientation (row 8 of Table 4.2). Applying (4.14), the error between the actual and estimated responses in Figure 4.5 is 0.0585 whereas the error between the actual and estimated responses in Figure 4.6 is 2.8007. In this case, aluminum ring would be selected as the target present which is indeed correct. Estimating the response $\mathbf{Y}$ using the poles from the other orientation of the large cylinder could be carried out; however, one would find the error to still be greater than 0.0585.

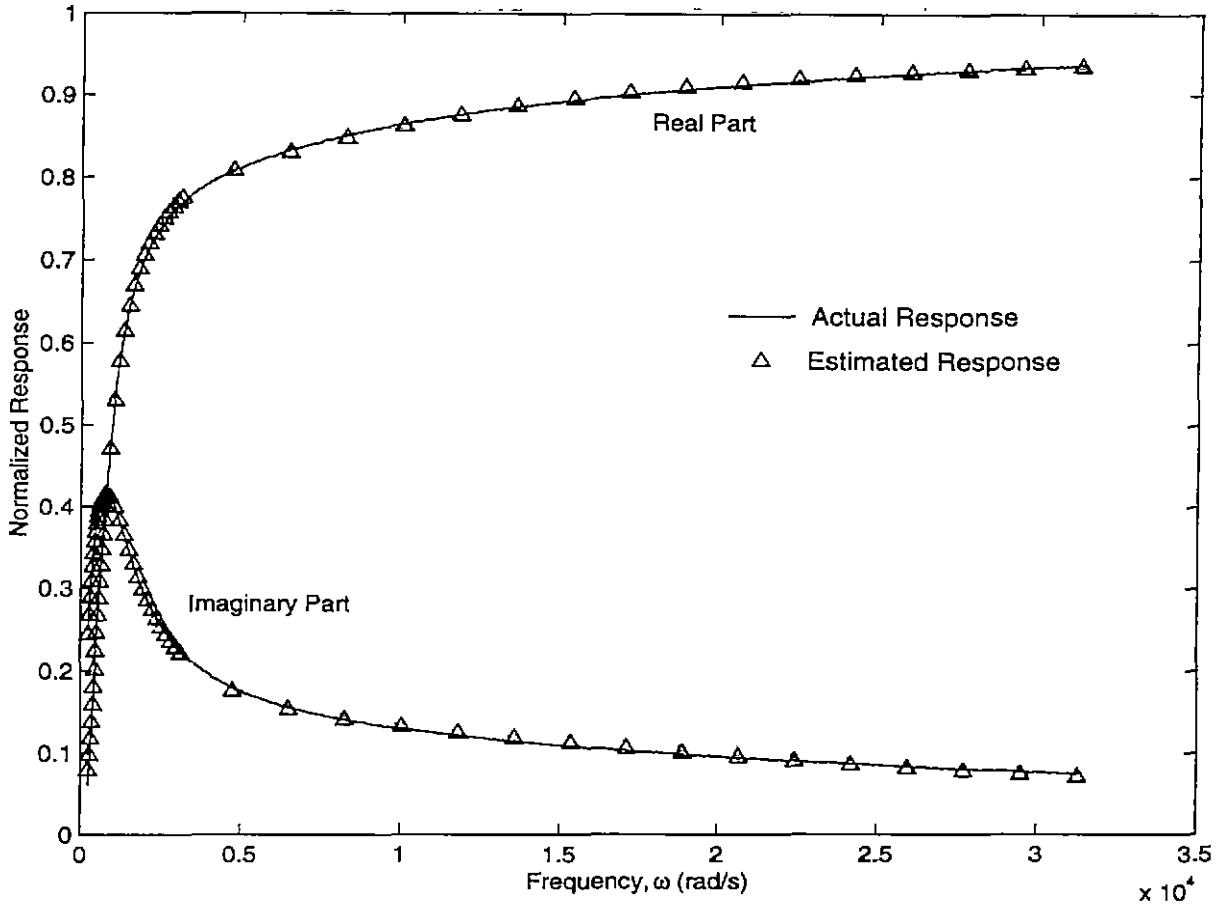

Figure 4.3. The response from the aluminum ring oriented with its open end perpendicular to the magnetic field. The estimated response was obtained using all the known poles of the aluminum ring.

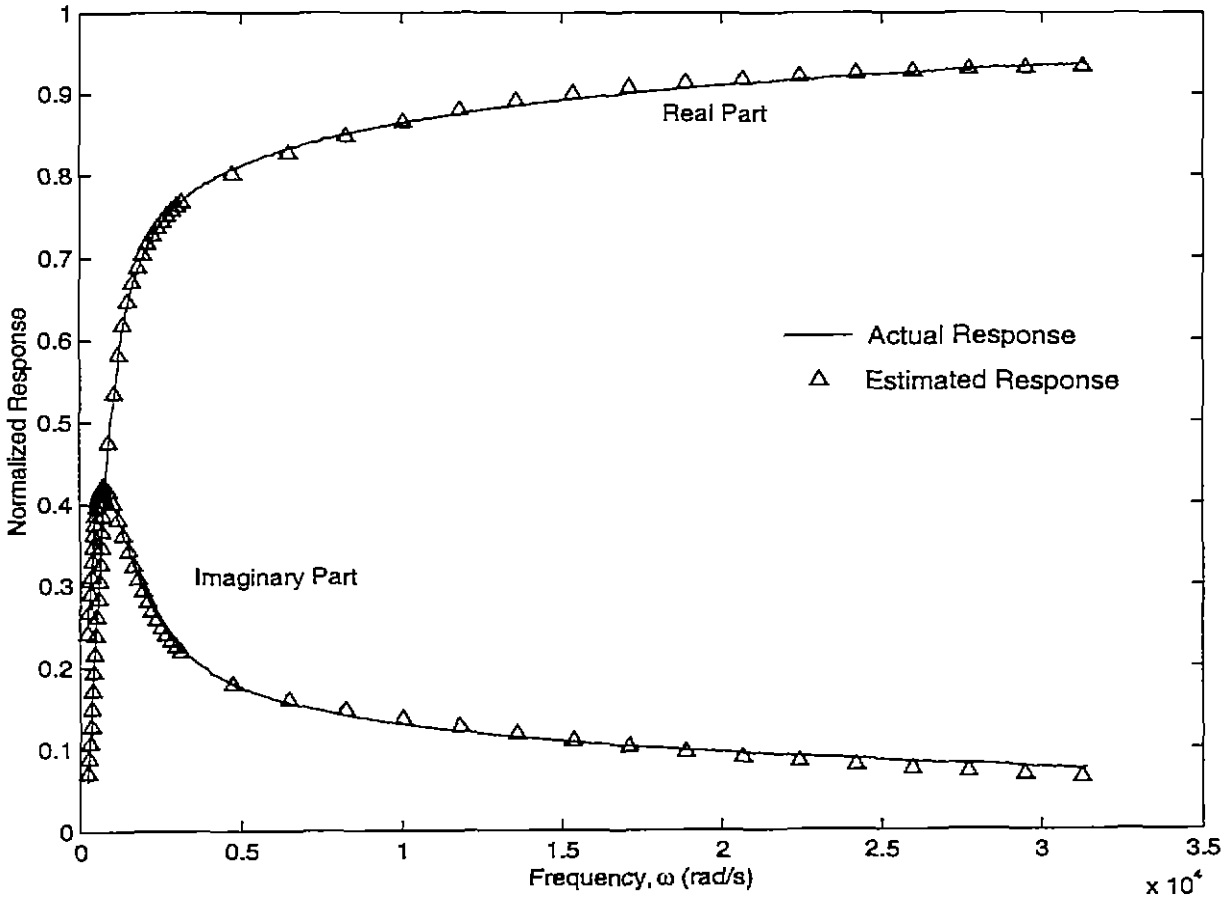

Figure 4.4. The response from the aluminum ring oriented with its open end perpendicular to the magnetic field. The estimated response was obtained using all the known poles of the large aluminum cylinder.

Target		Poles		
Description	Orientation w.r.t Magnetic Field			
Large Aluminum Block	⊥ to large side	3.1843e+02	1.7668e+03	1.2659e+04
	⊥ to medium side	3.9180e+02	2.2104e+03	1.3620e+04
	⊥ to small side	4.1076e+02	2.4240e+03	1.4198e+04
Square Aluminum Tube	⊥ to open end	1.0661e+03	1.9755e+04	
	⊥ to side of tube	1.0285e+03	5.6243e+03	2.1813e+04
Round Aluminum Ring	⊥ to open side	7.6673e+02	1.2808e+04	
	⊥ to side of ring	1.9256e+03	1.5028e+04	
Large Aluminum Cyl.	⊥ to end of cyl.	5.7490e+02	4.6849e+03	2.3477e+04
	⊥ to side of cyl.	5.5311e+02	4.0257e+03	2.1834e+04
Small Aluminum Cyl.	⊥ to end of cyl.	6.1187e+02	4.2525e+03	2.1018e+04
.	⊥ to side of cyl.	5.8373e+02	3.9326e+03	2.1053e+04
Thin Aluminum Cyl.	⊥ to end of cyl.	1.8771e+03	2.5441e+04	
.	⊥ to side of cyl.	1.4849e+03	1.5714e+04	
Copper Cylinder	⊥ to end of cyl.	2.3660e+02	1.3801e+03	1.0565e+04
	⊥ to side of cyl.	3.7929e+02	2.9885e+03	1.7441e+04

Table 4.2. The pole library organized by target description and orientation.

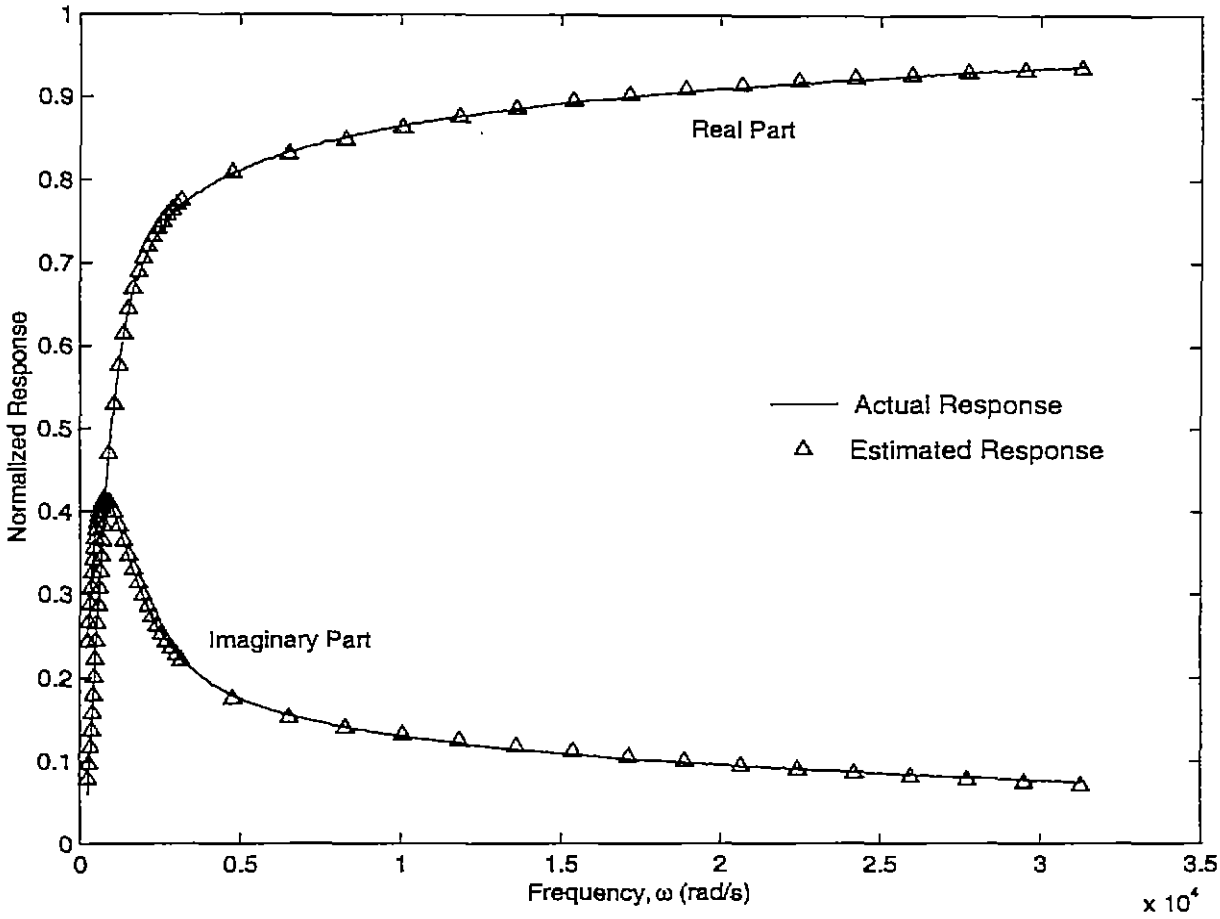

Figure 4.5. The response from the aluminum ring oriented with its open end perpendicular to the magnetic field. The estimated response was obtained using only the poles from line 6 of Table 4.2.

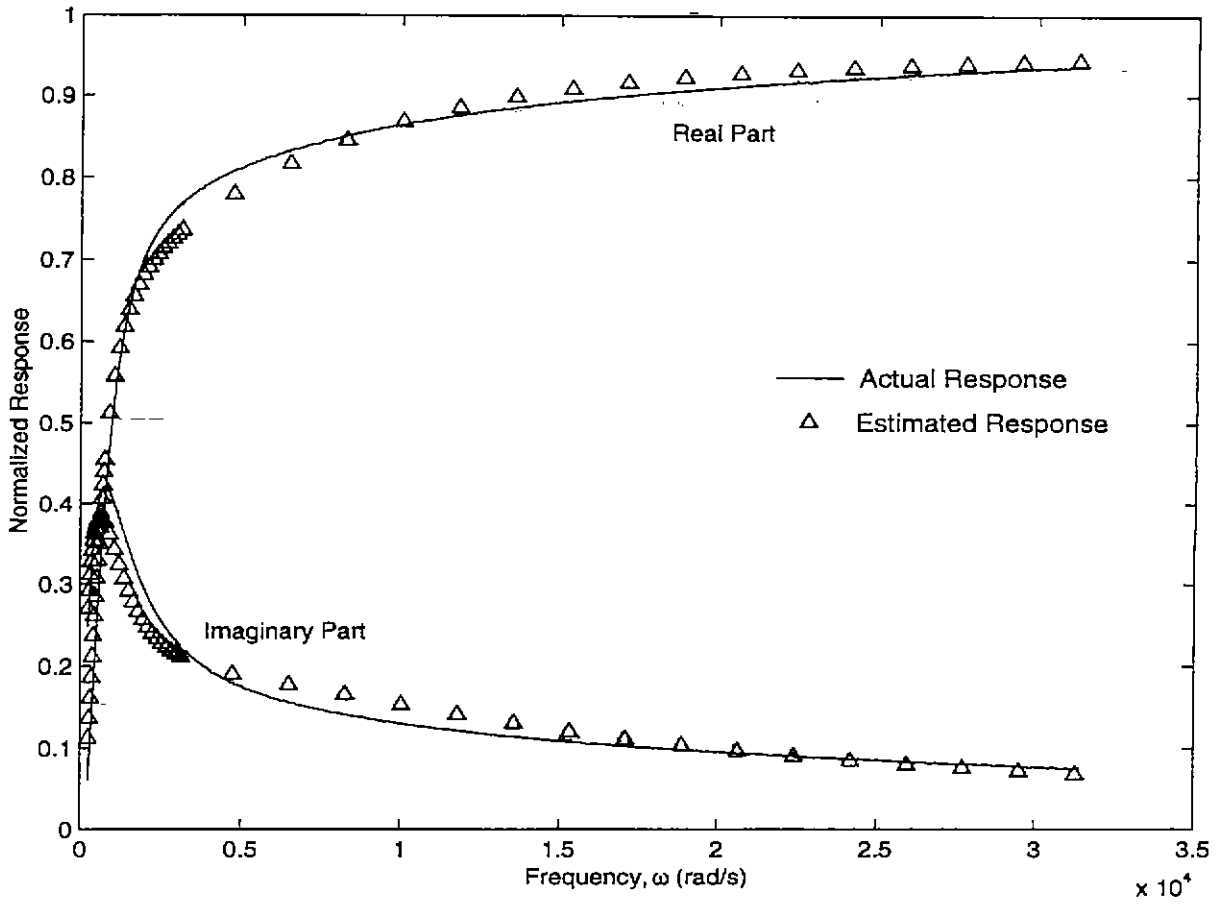

Figure 4.6. The response from the aluminum ring oriented with its open end perpendicular to the magnetic field. The estimated response was obtained using only the poles from line 8 of Table 4.2.

4.4 Results

Tables A.1 through A.17 in appendix A show the results of the identification algorithm for a large number of responses. For every object in Table 4.2, a response from each of the cardinal orientations was tested against the identification algorithm. In each case, the algorithm was able to select the correct target. The target whose poles produced the best estimate is highlighted in boldface in each of the tables.

Of the results displayed in Tables A.1 through A.15, there are two cases which produced some interesting numbers. The first case involves the response from either the large aluminum block or copper cylinder. In Tables A.1 through A.3 where the response is from the large aluminum block, one can see that the copper cylinder is competing with the large aluminum block for selection as the correct target. Similarly, in Tables A.14 and A.15 where the response is from the copper cylinder, the poles of the large aluminum block are producing good estimates. Although these two targets are made of different materials, their poles are very similar. As a result, discriminating between these two objects is difficult.

The next case of interest is when the response is from either the large aluminum cylinder or small aluminum cylinder. As shown in Tables A.8 and A.9, when the response is from the large aluminum cylinder, the small aluminum cylinder is competing for selection as the correct target. Similarly, in Tables A.10 and A.11 where the response is from the small aluminum cylinder, the poles of the large aluminum cylinder are producing good estimates of the actual response. This case simply illustrates the challenge in trying to discriminate among objects with slightly different characteristics.

Another interesting feature of the results can be observed in Tables A.6 and A.7. In these results, the measured response is from the aluminum ring. As discussed above, the wrong orientation of a particular target competes, in general, favorably with the correct orientation. However, this trend does not hold true for the aluminum ring because the poles for the two cardinal orientations are very different.

Tables A.16 and A.17 show the performance of the identification algorithm when the response is from an object in an arbitrary orientation. For the results displayed in Table A.16, the arbitrary response is from the large aluminum block. In this case, the identification selects the copper cylinder as the correct target. As stated earlier, the copper cylinder and aluminum block both have similar poles. When the response is from an arbitrary orientation of one of these two objects, there is enough similarity among the poles to produce an incorrect decision.

Table A.17 displays the results for the case when the response is from an arbitrary orientation of the large aluminum cylinder. In this case, the identification algorithm is able to select the correct target. However, the small cylinder, whose poles are similar to those of the large cylinder, is competing for selection as the correct target.

4.5 Algorithm Performance with Noisy Data for Various Pole Libraries

As stated earlier, the organization of the pole library is a critical part of the identification algorithm. When the pole library was organized such that the ML estimator was given too much freedom (e.g., too many poles were used to represent a given object), the identification algorithm was shown to perform poorly. Consequently, limiting the freedom of the ML estimator by reducing the number of poles used to represent an object improves the ID algorithm performance. This result intimates the following question: Why not limit the ML estimator further by representing each object's cardinal orientations by only one or two poles? In order to compare the performance of different library organizations, the algorithm was applied to noisy data for varying signal-to-noise ratios (SNR) through Monte Carlo simulations. The measured data contained some noise already (around 60dB SNR), and complex white Gaussian noise was generated and added to the measured data to give the appropriate SNR values. As a performance measure, the percent correct identifications for 1000 trials at each SNR value were recorded for libraries containing one, two, and three poles per object orientation. The library organization is illustrated for the three pole case in Table 4.2. (Note that some objects can only be represented by two poles.) Results of this simulation are shown in Figure 4.7. Note that the one pole representation performs better than either the two or three pole representations for all SNR values. This indicates that for the seven objects used in this simulation, a one pole representation provides the best discrimination capability.

In addition to the number of poles used to represent a particular object in the library, the organization of poles in the library also influences the performance of the ID algorithm. Recall the library organization shown in Table 4.1 performed poorly because the estimator was free to adjust *all* the coefficients such that any response could be fitted well. Theoretically, an object's cardinal orientation poles should be adequate to characterize the object in any orientation. When an object is oriented arbitrarily with respect to the applied magnetic field, the response can be represented as a linear combination of the cardinal orientation poles. Furthermore, the ratio of coefficients of the poles from a particular cardinal orientation should remain constant. For example, an object with a set of poles from one cardinal orientation given by σ_1 and σ_2 with a coefficient ratio, ρ_1, and a set of poles from a second cardinal orientation given by σ_3 and σ_4 with a coefficient ratio, ρ_2, can be represented as

$$F(\omega) = A_1 \left(\frac{j\omega}{\sigma_1 + j\omega} + \rho_1 \frac{j\omega}{\sigma_2 + j\omega} \right) + A_2 \left(\frac{j\omega}{\sigma_3 + j\omega} + \rho_2 \frac{j\omega}{\sigma_4 + j\omega} \right) \tag{4.15}$$

where A_1 and A_2 will vary depending on the orientation of the object. When the object is in a cardinal orientation, the coefficient for that set of poles will be a maximum and the other coefficient will be zero. Hence, there are now only two unknowns, A_1 and A_2, which should reduce the freedom of the ML estimator. With this in mind, the pole library was organized such that each object was represented by a single set of poles which are a combination of the objects' cardinal orientation poles as in Table 4.1. In addition, the

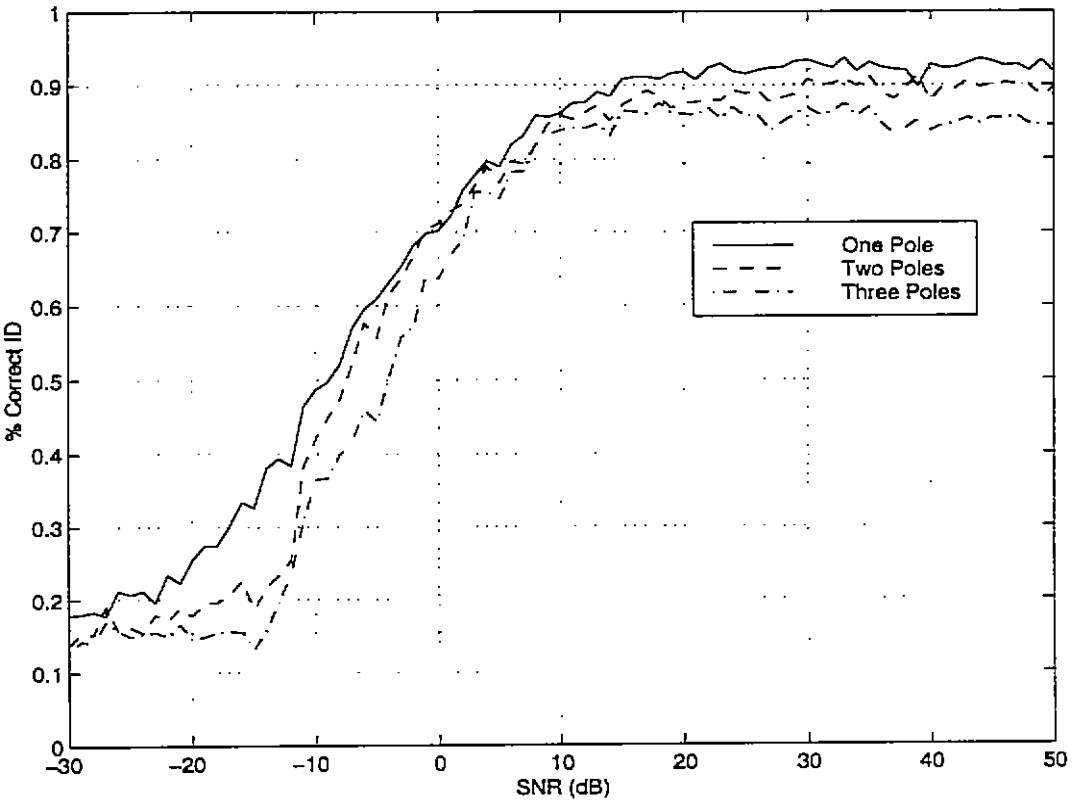

Figure 4.7. Performance of different library pole orders.

coefficient ratios from each of the cardinal orientations were included. Monte Carlo simulations were run to determine the relative performance of this approach. Figure 4.8 and Figure 4.9 show the performance of libraries containing one and two poles for each cardinal orientation, respectively. Note that the libraries containing cardinal pole sets separately perform better than those containing a single set of poles for each object. This result occurs despite the fact that pole coefficient ratios were known in the latter case. It is suspected that the reason for this is that there is still too much freedom in the ML estimator when using a single set of poles for each object. Accordingly, the best performance for a GLRT is still obtained when the pole library contains one pole per object orientation.

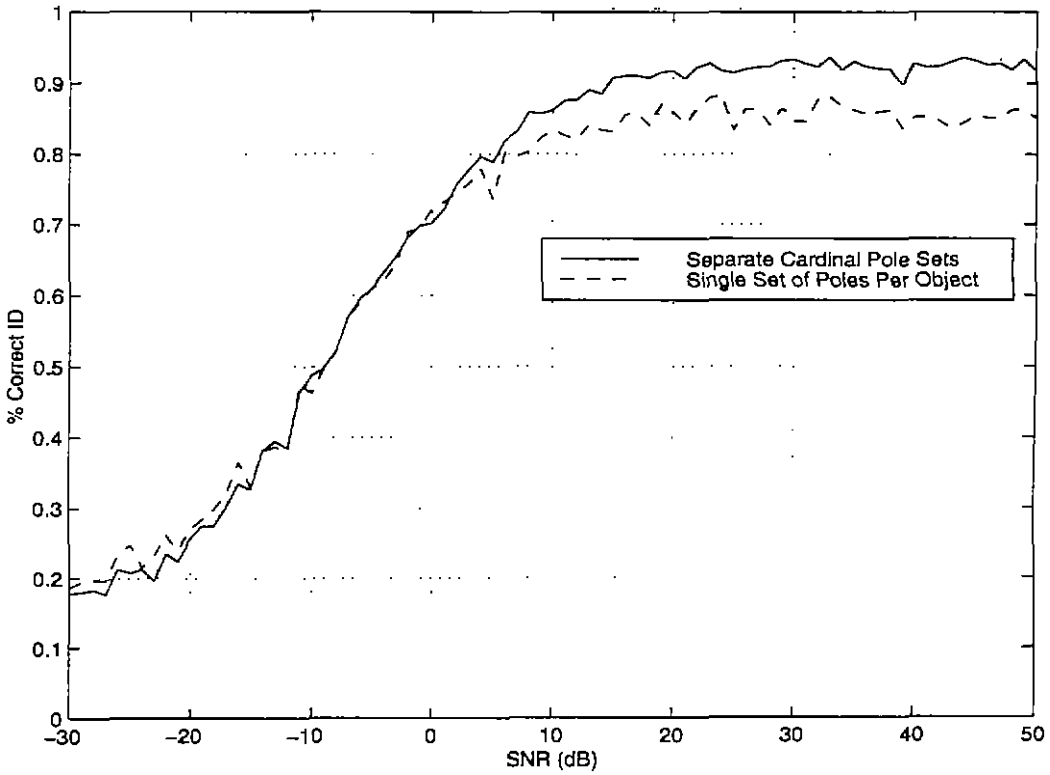

Figure 4.8. One pole representation comparison.

Improved performance over the one pole representation can be achieved, however, when information about the coefficients of the objects' poles are known. Knowledge of the objects' coefficients obviates the need to find ML estimates of the unknown parameters. Consequently, the GLRT can be replaced with a simple LRT, and the decision rule becomes equation (4.14) where the A_k's are known. For the coefficients to be known and constant for each measurement, an object's orientation and coupling between the object and receive coil must remain the same. This situation occurs when the measuring environment is the same for each measurement. To demonstrate the performance of this approach, only cardinal orientations of the

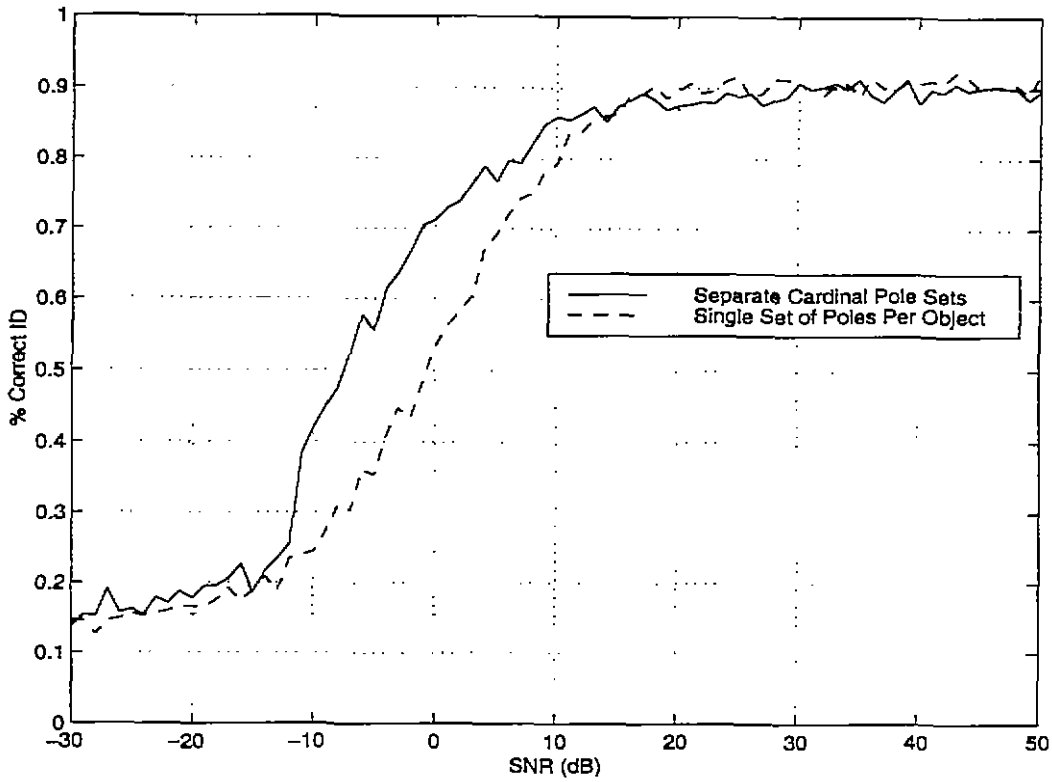

Figure 4.9. Two pole representation comparison.

objects were considered since the coefficients for arbitrary orientations were not known. The library was constructed such that each cardinal orientation of an object was represented by a single coefficient and pole. Results of a Monte Carlo simulation are shown in Figure 4.10. The performance of this approach exceeds that of any other and can be viewed as a best case scenario for the seven objects considered.

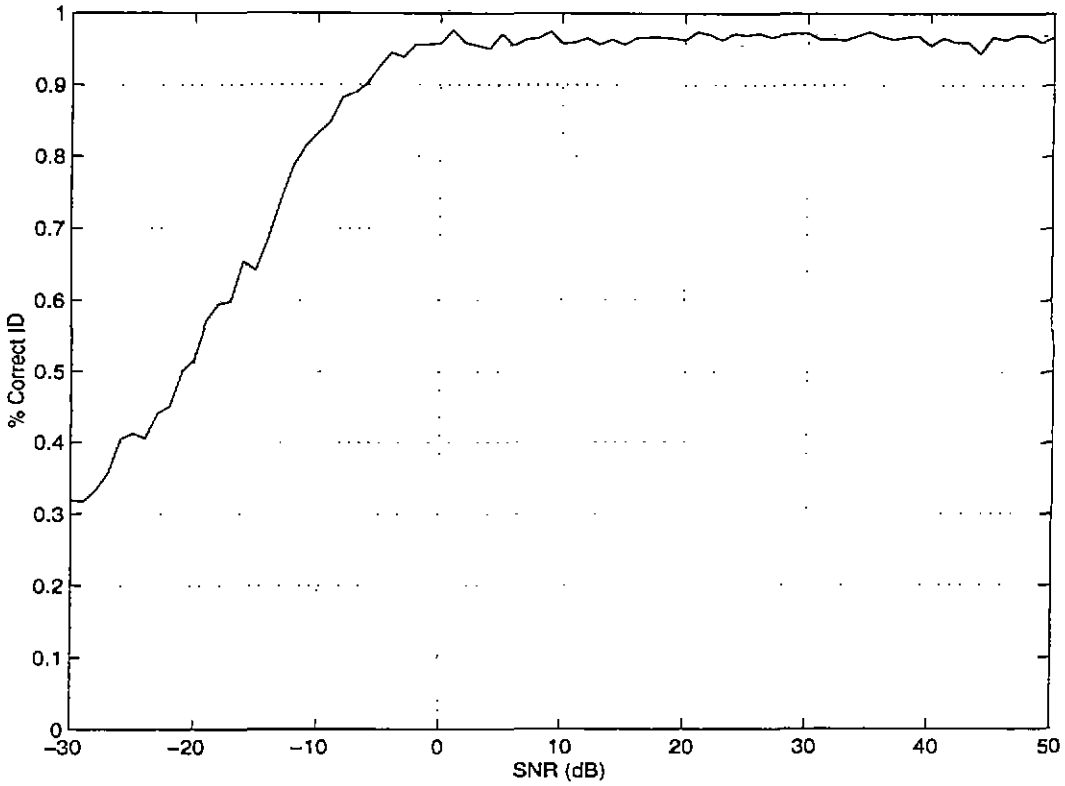

Figure 4.10. Performance of single pole cardinal orientations with known amplitudes.

5. Conclusion

This paper has demonstrated the feasibility of using metallic objects' low frequency responses as a means for object discrimination. The inherent challenge in using the low frequency response for discrimination results from the lack of structure in the response. It was discovered that most responses can be characterized within the tolerance of the noise by only two or three poles. Furthermore, from an identification standpoint, representing each object by only one pole (per cardinal orientation) provides the best performance. When information about the magnitude of each object's response is known, the ID algorithm provides almost perfect discrimination down to 0dB SNR. These results indicate that, as a general rule, limiting the freedom of the ID algorithm improves performance.

Further study is warranted to extend these results to smaller metallic objects such as those found in low-metal content anti-personnel mines. The challenge here lies in both measuring and extracting accurate poles from the response. The magnitude of the response from a small metal object will be small. and the decay rates (poles) will be large. From section 3.3, larger poles have larger variances which makes accurate pole extraction more difficult. Results from this paper could also be extended to permeable objects, such as the ferrous sphere described in section 2.

Appendix A. Tabular Results of Identification Algorithm

Poles		
Object	Orientation w.r.t Magnetic Field	$\| \mathbf{Y} - (\Phi_k + j\,\Psi_k)\,\hat{\mathbf{A}}_{k,\max} \|$
Large Aluminum Block	**Perpendicular to large side**	**0.4281**
Large Aluminum Block	Perpendicular to medium side	1.296
Large Aluminum Block	Perpendicular to small side	1.965
Square Aluminum Tube	Perpendicular to open end	43.20
Square Aluminum Tube	Perpendicular to side of tube	39.51
Round Aluminum Ring	Perpendicular to open side	18.89
Round Aluminum Ring	Perpendicular to side of ring	91.77
Large Aluminum Cyl.	Perpendicular to end of cyl.	8.116
Large Aluminum Cyl.	Perpendicular to side of cyl.	7.382
Small Aluminum Cyl.	Perpendicular to end of cyl.	10.89
Small Aluminum Cyl.	Perpendicular to side of cyl.	9.472
Thin Aluminium Cyl.	Perpendicular to end of cyl.	90.67
Thin Aluminium Cyl.	Perpendicular to side of cyl.	67.32
Copper Cylinder	Perpendicular to end of cyl.	2.219
Copper Cylinder	Perpendicular to side of cyl.	0.6825

Table A.1. The response $\mathbf{Y}$ is from the large aluminum block oriented with the large side of the block perpendicular to the magnetic field.

Poles		
Object	Orientation w.r.t Magnetic Field	$\| \mathbf{Y} - (\Phi_k + j\,\Psi_k)\,\hat{\mathbf{A}}_{k,\max} \|$
Large Aluminum Block	Perpendicular to large side	1.072
Large Aluminum Block	**Perpendicular to medium side**	**0.3129**
Large Aluminum Block	Perpendicular to small side	0.3994
Square Aluminum Tube	Perpendicular to open end	30.79
Square Aluminum Tube	Perpendicular to side of tube	27.76
Round Aluminum Ring	Perpendicular to open side	10.98
Round Aluminum Ring	Perpendicular to side of ring	74.52
Large Aluminum Cyl.	Perpendicular to end of cyl.	3.475
Large Aluminum Cyl.	Perpendicular to side of cyl.	3.044
Small Aluminum Cyl.	Perpendicular to end of cyl.	5.322
Small Aluminum Cyl.	Perpendicular to side of cyl.	4.395
Thin Aluminium Cyl.	Perpendicular to end of cyl.	73.30
Thin Aluminium Cyl.	Perpendicular to side of cyl.	52.16
Copper Cylinder	Perpendicular to end of cyl.	4.537
Copper Cylinder	Perpendicular to side of cyl.	0.4735

Table A.2. The response $\mathbf{Y}$ is from the large aluminum block oriented with the medium side of the block perpendicular to the magnetic field.

Poles		
Object	Orientation w.r.t Magnetic Field	$\| \mathbf{Y} - (\Phi_k + j\,\Psi_k)\,\hat{\mathbf{A}}_{k,\max} \|$
Large Aluminum Block	Perpendicular to large side	1.572
Large Aluminum Block	Perpendicular to medium side	0.3796
Large Aluminum Block	**Perpendicular to small side**	**0.2974**
Square Aluminum Tube	Perpendicular to open end	24.26
Square Aluminum Tube	Perpendicular to side of tube	23.77
Round Aluminum Ring	Perpendicular to open side	8.811
Round Aluminum Ring	Perpendicular to side of ring	68.70
Large Aluminum Cyl.	Perpendicular to end of cyl.	2.416
Large Aluminum Cyl.	Perpendicular to side of cyl.	2.081
Small Aluminum Cyl.	Perpendicular to end of cyl.	3.955
Small Aluminum Cyl.	Perpendicular to side of cyl.	3.189
Thin Aluminium Cyl.	Perpendicular to end of cyl.	67.41
Thin Aluminium Cyl.	Perpendicular to side of cyl.	47.19
Copper Cylinder	Perpendicular to end of cyl.	5.357
Copper Cylinder	Perpendicular to side of cyl.	0.7473

Table A.3. The response $\mathbf{Y}$ is from the large aluminum block oriented with the small side of the block perpendicular to the magnetic field.

Poles		
Object	Orientation w.r.t Magnetic Field	$\| \mathbf{Y} - (\Phi_k + j\,\Psi_k)\,\hat{\mathbf{A}}_{k,\max} \|$
Large Aluminum Block	Perpendicular to large side	22.52
Large Aluminum Block	Perpendicular to medium side	26.11
Large Aluminum Block	Perpendicular to small side	24.34
Square Aluminum Tube	**Perpendicular to open end**	**0.1521**
Square Aluminum Tube	Perpendicular to side of tube	0.2661
Round Aluminum Ring	Perpendicular to open side	7.180
Round Aluminum Ring	Perpendicular to side of ring	19.06
Large Aluminum Cyl.	Perpendicular to end of cyl.	14.90
Large Aluminum Cyl.	Perpendicular to side of cyl.	15.24
Small Aluminum Cyl.	Perpendicular to end of cyl.	11.65
Small Aluminum Cyl.	Perpendicular to side of cyl.	12.70
Thin Aluminium Cyl.	Perpendicular to end of cyl.	18.47
Thin Aluminium Cyl.	Perpendicular to side of cyl.	5.562
Copper Cylinder	Perpendicular to end of cyl.	28.64
Copper Cylinder	Perpendicular to side of cyl.	27.35

Table A.4. The response $\mathbf{Y}$ is from the square aluminum tube oriented with the open end of the tube perpendicular to the magnetic field.

Poles		
Object	Orientation w.r.t Magnetic Field	$\| \mathbf{Y} - (\Phi_k + j\,\Psi_k)\,\hat{\mathbf{A}}_{k,\max} \|$
Large Aluminum Block	Perpendicular to large side	22.52
Large Aluminum Block	Perpendicular to medium side	19.41
Large Aluminum Block	Perpendicular to small side	17.99
Square Aluminum Tube	Perpendicular to open end	0.1582
Square Aluminum Tube	**Perpendicular to side of tube**	**0.0536**
Round Aluminum Ring	Perpendicular to open side	4.881
Round Aluminum Ring	Perpendicular to side of ring	18.48
Large Aluminum Cyl.	Perpendicular to end of cyl.	10.51
Large Aluminum Cyl.	Perpendicular to side of cyl.	10.72
Small Aluminum Cyl.	Perpendicular to end of cyl.	7.934
Small Aluminum Cyl.	Perpendicular to side of cyl.	8.719
Thin Aluminium Cyl.	Perpendicular to end of cyl.	17.42
Thin Aluminium Cyl.	Perpendicular to side of cyl.	5.840
Copper Cylinder	Perpendicular to end of cyl.	21.64
Copper Cylinder	Perpendicular to side of cyl.	20.39

Table A.5. The response $\mathbf{Y}$ is from the square aluminum tube oriented with the side of the tube perpendicular to the magnetic field.

Poles		
Object	Orientation w.r.t Magnetic Field	$\| \mathbf{Y} - (\Phi_k + j\,\Psi_k)\,\hat{\mathbf{A}}_{k,\max} \|$
Large Aluminum Block	Perpendicular to large side	17.17
Large Aluminum Block	Perpendicular to medium side	11.72
Large Aluminum Block	Perpendicular to small side	9.934
Square Aluminum Tube	Perpendicular to open end	8.429
Square Aluminum Tube	Perpendicular to side of tube	6.392
Round Aluminum Ring	***Perpendicular to open side***	***0.0584***
Round Aluminum Ring	Perpendicular to side of ring	51.08
Large Aluminum Cyl.	Perpendicular to end of cyl.	2.800
Large Aluminum Cyl.	Perpendicular to side of cyl.	3.226
Small Aluminum Cyl.	Perpendicular to end of cyl.	1.410
Small Aluminum Cyl.	Perpendicular to side of cyl.	1.997
Thin Aluminium Cyl.	Perpendicular to end of cyl.	50.41
Thin Aluminium Cyl.	Perpendicular to side of cyl.	26.97
Copper Cylinder	Perpendicular to end of cyl.	22.89
Copper Cylinder	Perpendicular to side of cyl.	13.99

Table A.6. The response $\mathbf{Y}$ is from the round aluminum ring oriented with the open side of the ring perpendicular to the magnetic field.

Poles		
Object	Orientation w.r.t Magnetic Field	$\| \mathbf{Y} - (\Phi_k + j\,\Psi_k)\,\hat{\mathbf{A}}_{k,\max} \|$
Large Aluminum Block	Perpendicular to large side	13.14
Large Aluminum Block	Perpendicular to medium side	15.14
Large Aluminum Block	Perpendicular to small side	15.30
Square Aluminum Tube	Perpendicular to open end	10.36
Square Aluminum Tube	Perpendicular to side of tube	8.323
Round Aluminum Ring	Perpendicular to open side	17.45
Round Aluminum Ring	**Perpendicular to side of ring**	**0.3440**
Large Aluminum Cyl.	Perpendicular to end of cyl.	14.76
Large Aluminum Cyl.	Perpendicular to side of cyl.	13.72
Small Aluminum Cyl.	Perpendicular to end of cyl.	12.89
Small Aluminum Cyl.	Perpendicular to side of cyl.	12.50
Thin Aluminium Cyl.	Perpendicular to end of cyl.	0.8575
Thin Aluminium Cyl.	Perpendicular to side of cyl.	2.375
Copper Cylinder	Perpendicular to end of cyl.	7.105
Copper Cylinder	Perpendicular to side of cyl.	13.45

Table A.7. The response $\mathbf{Y}$ is from the round aluminum ring oriented with the side of the ring perpendicular to the magnetic field.

Poles		
Object	Orientation w.r.t Magnetic Field	$\| \mathbf{Y} - (\Phi_k + j\,\Psi_k)\,\hat{\mathbf{A}}_{k,\max} \|$
Large Aluminum Block	Perpendicular to large side	7.391
Large Aluminum Block	Perpendicular to medium side	3.631
Large Aluminum Block	Perpendicular to small side	2.622
Square Aluminum Tube	Perpendicular to open end	19.31
Square Aluminum Tube	Perpendicular to side of tube	16.35
Round Aluminum Ring	Perpendicular to open side	2.944
Round Aluminum Ring	Perpendicular to side of ring	68.50
Large Aluminum Cyl.	**Perpendicular to end of cyl.**	**0.1874**
Large Aluminum Cyl.	Perpendicular to side of cyl.	0.2075
Small Aluminum Cyl.	Perpendicular to end of cyl.	0.4548
Small Aluminum Cyl.	Perpendicular to side of cyl.	0.2752
Thin Aluminium Cyl.	Perpendicular to end of cyl.	67.39
Thin Aluminium Cyl.	Perpendicular to side of cyl.	42.20
Copper Cylinder	Perpendicular to end of cyl.	13.33
Copper Cylinder	Perpendicular to side of cyl.	5.148

Table A.8. The response $\mathbf{Y}$ is from the large aluminum cylinder oriented with the end of the cylinder perpendicular to the magnetic field.

Poles		$\| \mathbf{Y} - (\Phi_k + j\,\Psi_k)\,\hat{\mathbf{A}}_{k,\max} \|$
Object	Orientation w.r.t Magnetic Field	
Large Aluminum Block	Perpendicular to large side	6.433
Large Aluminum Block	Perpendicular to medium side	3.079
Large Aluminum Block	Perpendicular to small side	2.193
Square Aluminum Tube	Perpendicular to open end	19.24
Square Aluminum Tube	Perpendicular to side of tube	16.43
Round Aluminum Ring	Perpendicular to open side	3.246
Round Aluminum Ring	Perpendicular to side of ring	67.01
Large Aluminum Cyl.	Perpendicular to end of cyl.	0.2577
Large Aluminum Cyl.	**Perpendicular to side of cyl.**	**0.2388**
Small Aluminum Cyl.	Perpendicular to end of cyl.	0.6270
Small Aluminum Cyl.	Perpendicular to side of cyl.	0.3979
Thin Aluminium Cyl.	Perpendicular to end of cyl.	65.71
Thin Aluminium Cyl.	Perpendicular to side of cyl.	41.48
Copper Cylinder	Perpendicular to end of cyl.	11.82
Copper Cylinder	Perpendicular to side of cyl.	4.409

Table A.9. The response $\mathbf{Y}$ is from the large aluminum cylinder oriented with the side of the cylinder perpendicular to the magnetic field.

Poles		
Object	Orientation w.r.t Magnetic Field	$\| \mathbf{Y} - (\Phi_k + j\,\Psi_k)\,\hat{\mathbf{A}}_{k,\max} \|$
Large Aluminum Block	Perpendicular to large side	8.308
Large Aluminum Block	Perpendicular to medium side	4.760
Large Aluminum Block	Perpendicular to small side	3.709
Square Aluminum Tube	Perpendicular to open end	12.78
Square Aluminum Tube	Perpendicular to side of tube	10.63
Round Aluminum Ring	Perpendicular to open side	1.273
Round Aluminum Ring	Perpendicular to side of ring	53.66
Large Aluminum Cyl.	Perpendicular to end of cyl.	0.4017
Large Aluminum Cyl.	Perpendicular to side of cyl.	0.5063
Small Aluminum Cyl.	**Perpendicular to end of cyl.**	**0.1653**
Small Aluminum Cyl.	Perpendicular to side of cyl.	0.2102
Thin Aluminium Cyl.	Perpendicular to end of cyl.	52.34
Thin Aluminium Cyl.	Perpendicular to side of cyl.	31.32
Copper Cylinder	Perpendicular to end of cyl.	13.01
Copper Cylinder	Perpendicular to side of cyl.	6.179

Table A.10. The response $\mathbf{Y}$ is from the small aluminum cylinder oriented with the end of the cylinder perpendicular to the magnetic field.

Poles		$\| \mathbf{Y} - (\Phi_k + j\,\Psi_k)\,\hat{\mathbf{A}}_{k,\max} \|$
Object	Orientation w.r.t Magnetic Field	
Large Aluminum Block	Perpendicular to large side	7.297
Large Aluminum Block	Perpendicular to medium side	3.988
Large Aluminum Block	Perpendicular to small side	3.036
Square Aluminum Tube	Perpendicular to open end	14.14
Square Aluminum Tube	Perpendicular to side of tube	11.91
Round Aluminum Ring	Perpendicular to open side	1.795
Round Aluminum Ring	Perpendicular to side of ring	55.71
Large Aluminum Cyl.	Perpendicular to end of cyl.	0.3007
Large Aluminum Cyl.	Perpendicular to side of cyl.	0.3561
Small Aluminum Cyl.	Perpendicular to end of cyl.	0.2570
Small Aluminum Cyl.	**Perpendicular to side of cyl.**	**0.2122**
Thin Aluminium Cyl.	Perpendicular to end of cyl.	54.33
Thin Aluminium Cyl.	Perpendicular to side of cyl.	33.13
Copper Cylinder	Perpendicular to end of cyl.	11.93
Copper Cylinder	Perpendicular to side of cyl.	5.297

Table A.11. The response $\mathbf{Y}$ is from the small aluminum cylinder oriented with the side of the cylinder perpendicular to the magnetic field.

Poles		
Object	Orientation w.r.t Magnetic Field	$\| \mathbf{Y} - (\Phi_k + j\,\Psi_k)\,\hat{\mathbf{A}}_{k,\max} \|$
Large Aluminum Block	Perpendicular to large side	32.29
Large Aluminum Block	Perpendicular to medium side	34.17
Large Aluminum Block	Perpendicular to small side	33.96
Square Aluminum Tube	Perpendicular to open end	19.01
Square Aluminum Tube	Perpendicular to side of tube	16.15
Round Aluminum Ring	Perpendicular to open side	29.66
Round Aluminum Ring	Perpendicular to side of ring	6.059
Large Aluminum Cyl.	Perpendicular to end of cyl.	30.71
Large Aluminum Cyl.	Perpendicular to side of cyl.	29.73
Small Aluminum Cyl.	Perpendicular to end of cyl.	27.64
Small Aluminum Cyl.	Perpendicular to side of cyl.	27.62
Thin Aluminium Cyl.	**Perpendicular to end of cyl.**	**5.707**
Thin Aluminium Cyl.	Perpendicular to side of cyl.	7.510
Copper Cylinder	Perpendicular to end of cyl.	22.32
Copper Cylinder	Perpendicular to side of cyl.	32.30

Table A.12. The response $\mathbf{Y}$ is from the thin aluminum cylinder oriented with the side of the cylinder perpendicular to the magnetic field.

Poles		
Object	Orientation w.r.t Magnetic Field	$\| \mathbf{Y} - (\Phi_k + j\,\Psi_k)\,\hat{\mathbf{A}}_{k,max} \|$
Large Aluminum Block	Perpendicular to large side	22.48
Large Aluminum Block	Perpendicular to medium side	22.47
Large Aluminum Block	Perpendicular to small side	21.87
Square Aluminum Tube	Perpendicular to open end	6.424
Square Aluminum Tube	Perpendicular to side of tube	4.832
Round Aluminum Ring	Perpendicular to open side	14.73
Round Aluminum Ring	Perpendicular to side of ring	3.794
Large Aluminum Cyl.	Perpendicular to end of cyl.	17.44
Large Aluminum Cyl.	Perpendicular to side of cyl.	16.99
Small Aluminum Cyl.	Perpendicular to end of cyl.	14.81
Small Aluminum Cyl.	Perpendicular to side of cyl.	15.10
Thin Aluminium Cyl.	Perpendicular to end of cyl.	2.877
Thin Aluminium Cyl.	**Perpendicular to side of cyl.**	**0.9446**
Copper Cylinder	Perpendicular to end of cyl.	15.10
Copper Cylinder	Perpendicular to side of cyl.	16.82

Table A.13. The response $\mathbf{Y}$ is from the thin aluminum cylinder oriented with the side of the cylinder perpendicular to the magnetic field.

Poles		
Object	Orientation w.r.t Magnetic Field	$\| \mathbf{Y} - (\Phi_k + j\,\Psi_k)\,\hat{\mathbf{A}}_{k,\max} \|$
Large Aluminum Block	Perpendicular to large side	3.969
Large Aluminum Block	Perpendicular to medium side	9.807
Large Aluminum Block	Perpendicular to small side	12.21
Square Aluminum Tube	Perpendicular to open end	86.08
Square Aluminum Tube	Perpendicular to side of tube	79.97
Round Aluminum Ring	Perpendicular to open side	47.95
Round Aluminum Ring	Perpendicular to side of ring	152.8
Large Aluminum Cyl.	Perpendicular to end of cyl.	27.37
Large Aluminum Cyl.	Perpendicular to side of cyl.	25.66
Small Aluminum Cyl.	Perpendicular to end of cyl.	32.69
Small Aluminum Cyl.	Perpendicular to side of cyl.	29.82
Thin Aluminium Cyl.	Perpendicular to end of cyl.	152.2
Thin Aluminium Cyl.	Perpendicular to side of cyl.	119.9
Copper Cylinder	**Perpendicular to end of cyl.**	**0.3676**
Copper Cylinder	Perpendicular to side of cyl.	6.752

Table A.14. The response $\mathbf{Y}$ is from copper cylinder oriented with the end of the cylinder perpendicular to the magnetic field.

Poles		
Object	Orientation w.r.t Magnetic Field	$\| \mathbf{Y} - (\Phi_k + j\,\Psi_k)\,\hat{\mathbf{A}}_{k,\max} \|$
Large Aluminum Block	Perpendicular to large side	0.5725
Large Aluminum Block	Perpendicular to medium side	0.4810
Large Aluminum Block	Perpendicular to small side	0.9416
Square Aluminum Tube	Perpendicular to open end	44.58
Square Aluminum Tube	Perpendicular to side of tube	40.25
Round Aluminum Ring	Perpendicular to open side	17.97
Round Aluminum Ring	Perpendicular to side of ring	99.63
Large Aluminum Cyl.	Perpendicular to end of cyl.	6.665
Large Aluminum Cyl.	Perpendicular to side of cyl.	5.911
Small Aluminum Cyl.	Perpendicular to end of cyl.	9.435
Small Aluminum Cyl.	Perpendicular to side of cyl.	7.982
Thin Aluminium Cyl.	Perpendicular to end of cyl.	98.83
Thin Aluminium Cyl.	Perpendicular to side of cyl.	71.70
Copper Cylinder	Perpendicular to end of cyl.	4.860
Copper Cylinder	**Perpendicular to side of cyl.**	**0.2389**

Table A.15. The response $\mathbf{Y}$ is from the small aluminum cylinder oriented with the side of the cylinder perpendicular to the magnetic field.

Poles		
Object	Orientation w.r.t Magnetic Field	$\| \mathbf{Y} - (\Phi_k + j\,\Psi_k)\,\hat{\mathbf{A}}_{k,max} \|$
Large Aluminum Block	Perpendicular to large side	0.5855
Large Aluminum Block	Perpendicular to medium side	0.6142
Large Aluminum Block	Perpendicular to small side	0.9744
Square Aluminum Tube	Perpendicular to open end	32.78
Square Aluminum Tube	Perpendicular to side of tube	29.69
Round Aluminum Ring	Perpendicular to open side	14.30
Round Aluminum Ring	Perpendicular to side of ring	81.04
Large Aluminum Cyl.	Perpendicular to end of cyl.	5.435
Large Aluminum Cyl.	Perpendicular to side of cyl.	4.874
Small Aluminum Cyl.	Perpendicular to end of cyl.	7.682
Small Aluminum Cyl.	Perpendicular to side of cyl.	6.549
Thin Aluminium Cyl.	Perpendicular to end of cyl.	79.85
Thin Aluminium Cyl.	Perpendicular to side of cyl.	58.08
Copper Cylinder	Perpendicular to end of cyl.	3.180
Copper Cylinder	**Perpendicular to side of cyl.**	**0.4056**

Table A.16. The response $\mathbf{Y}$ is from the large aluminum block in an arbitrary orientation.

Poles		
Object	Orientation w.r.t Magnetic Field	$\| \mathbf{Y} - (\Phi_k + j\,\Psi_k)\,\hat{\mathbf{A}}_{k,\max} \|$
Large Aluminum Block	Perpendicular to large side	7.187
Large Aluminum Block	Perpendicular to medium side	3.608
Large Aluminum Block	Perpendicular to small side	2.633
Square Aluminum Tube	Perpendicular to open end	17.86
Square Aluminum Tube	Perpendicular to side of tube	15.12
Round Aluminum Ring	Perpendicular to open side	2.624
Round Aluminum Ring	Perpendicular to side of ring	64.85
Large Aluminum Cyl.	**Perpendicular to end of cyl.**	**0.1883**
Large Aluminum Cyl.	Perpendicular to side of cyl.	0.2147
Small Aluminum Cyl.	Perpendicular to end of cyl.	0.3885
Small Aluminum Cyl.	Perpendicular to side of cyl.	0.2397
Thin Aluminium Cyl.	Perpendicular to end of cyl.	63.62
Thin Aluminium Cyl.	Perpendicular to side of cyl.	39.63
Copper Cylinder	Perpendicular to end of cyl.	12.68
Copper Cylinder	Perpendicular to side of cyl.	5.043

Table A.17. The response $\mathbf{Y}$ is from the large aluminum cylinder in an arbitrary orientation.

References

1. C.E. Baum, Low-Frequency Near-Field Magnetic Scattering from Highly, But Not Perfectly Conducting Bodies, Interaction Note 499, November 1993.

2. C.E. Baum, On the Singularity Expansion Method for the Solution of Electromagnetic Interaction Problems, Interaction Note 88, December 1971.

3. C.E. Baum, Norbert Geng, and Lawrence Carin, Integral Equations and Polarizability for Magnetic Singularity Identification, Interaction Note 524, March 1997.

4. G.D. Sower, Eddy Current Responses of Canonical Metallic Targets - Theory and Measurements, Interaction Note 526, May 1997.

5. C.E. Baum, Two-Dimensional Coils for Low-Frequency Magnetic Illumination and Detection, Sensor and Simulation Note 406, November 1996.

6. C.E. Baum, Symmetry in Electromagnetic Scattering as a Target Discriminant, Interaction Note 523. October 1996.

7. Rev. T. Bayes, "An essay toward solving a problem in the doctrine of chance, " *Philos, Trans. R. Soc. London*, Vol. 53, 370-418, 1763; reprinted in *Biometrika*, Vol. 45, 293-315, 1958.

8. E.T. Jaynes and C.R. Smith , "Theory of radar target discrimination," Technical Report RD-AS-96-6, Procurement Instrument Identification Number DAAL03-86-D-001, D.O. 1515, Commander, US Army Missile Command, ATTN: AMSMI-RD-AS-RA, Redstone Arsenal, AL 35898-5253, February 1991.

9. Y. Das, J.E. McFee, J. Toews, and G.C. Stuart, "Analysis of an electromagnetic induction detector for real-time location of buried objects," *IEEE Transactions on Geoscience and Remote Sensing*, Vol. 28, no. 3, pp. 278-288, May 1990..

10. A.H. Trang, P.V. Czipott, D.A. Waldron, "Characterization of small metallic objects and non-metallic anti-personnel mines," Published by SPIE, Volume 3079, April 1997.

11. M. L. Van Blaricum and R. Mittra, "A technique for extracting the poles and residues of a system directly from its transient response," *IEEE Transactions on Antennas and Propagation*, Vol. AP-23, no. 6, pp. 777-781, Nov. 1975.

12. E. M. Dowling, R. D. DeGroat, and D. A. Linebarger, "Exponential parameter estimation in the presence of known components and noise," *IEEE Transactions on Antennas and Propagation*, Vol. 42, no. 5, pp. 590-599, May 1994.

13. T. K. Sarkar and O. Pereira, "Using the matrix pencil method to estimate the parameters of a sum of complex exponentials," *IEEE Antennas and Propagation Magazine*, Vol. 37, no. 1, pp. 48-55, Feb. 1995.

14. G. T. Chapman and D. B. Kirk, "A method for extracting aerodynamic coefficients from free-flight data," *AIAA Journal*, Vol. 8, no. 4, pp. 753-758, Apr. 1970.

15. R. L. Haupt, "An introduction to genetic algorithms for electromagnetics," *IEEE Antennas and Propagation Magazine*, Vol. 37, no. 2, pp. 7-15, Apr. 1995.

16. Y. Bresler and A. Macovski, "Exact maximum likelihood parameter estimation of superimposed exponential signals in noise," *IEEE Transactions on Acoustics, Speech, and Signal Processing*, Vol. ASSP-34, no. 5, pp. 1081-1089, Oct. 1986.

17. G.L. Bretthorst, *Bayesian Spectrum Analysis and Parameter Estimation.* Springer-Verlag, 1988.

18. S.M. Kay, *Fundamentals of Statistical Signal Processing.* Prentice Hall, 1993.

19. H.L. VanTrees, *Detection, Estimation, and Modulation Theory.* John Wiley & Sons, 1968.

20. H.V. Poor, *An Introduction to Signal Detection and Estimation*. Springer-Verlag, 2nd ed., 1994.

21. M.D. Srinath, P.K. Rajesekaran, and R. Viswanathan, *Introduction to Statistical Signal Processing with Applications*. Prentice Hall, 1996.

22. S.M. Kay, *Modern Spectral Estimation*. Prentice Hall, 1988.